# Cross-Correlation Digital Particle Image Velocimetry – A Review

*by*

Dana Dabiri

Department of Aeronautics & Astronautics
Box 352400
University of Washington
Seattle, WA, 98195

# 1 INTRODUCTION

The dream of experimental fluid dynamicists is to be able to measure complex, three-dimensional turbulent flow fields globally with very high spatial and temporal resolution. While we are still far from fully realizing this dream, significant progress has been made towards this goal during the last two decades. Early quantitative measurement methods using Pitot tubes, Venturi tubes and later measurement methods, such as Hot Wire Anemometry (HWA) and Laser-Doppler Anemometry (LDA), by their nature, were measurement methods that provided instantaneous velocity signals at single-points through time (see Figure 1). As can be seen from typical data such as those shown in Figure 1a, early emphasis in turbulence research and its theoretical advancement necessitated a statistical description of turbulent flow fields, which relied heavily upon measurements provided by these single-point measurement techniques. Though useful, these statistical single point descriptions could not give us a clear instantaneous picture of what the fluid was doing globally, and how its instantaneous physics ultimately result in the fluid's statistical behavior.

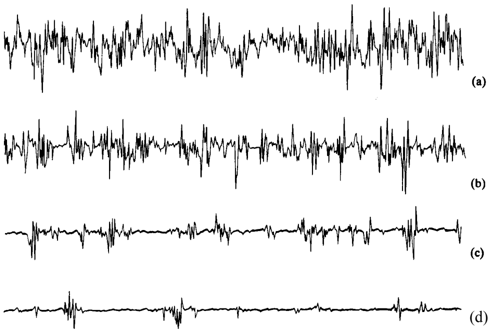

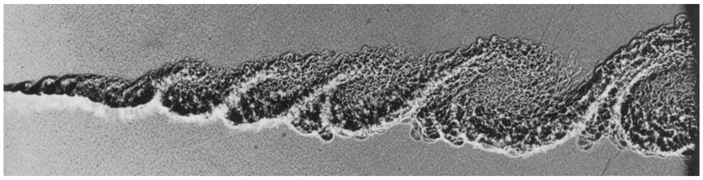

Figure 1: Left: Single-point measurements at various locations of a turbulent wake flow, Re=6500, x/d=28, y/d = a)0.87 b)2.25 c)3.4 d)4.2[1] Right: Shadowgraph of a turbulent shear layer revealing several levels of large coherent structures[2]

Since the early seventies, the discovery of the existence of three-dimensional coherent structures within turbulent flows[2] (see Figure 1b) using qualitative flow visualization methods (i.e. shadowgraphs, Schlieren systems, dye injection, etc) has been of significant interest for turbulence researchers. While flow visualization techniques have been around since the days of Prandtl, it is only recently that the advent of modern imaging, laser, and data acquisition technology has allowed for *qualitative* flow visualization to become *quantitative*. These advents have allowed for the development and advancement of a relatively new measurement technique, Particle Image Velocimetry (PIV), specifically its digital implementation, which allows for the global measurements of two-component velocities within a two-dimensional domain through time. Because of its ability to provide global two-dimensional kinematic information as well as its ability to map the evolution of coherent structures through time, PIV has become a powerful tool in studying, understanding, and modeling fluid flow behavior. This chapter is therefore dedicated to reviewing digital PIV, specifically its most widely used implementation, cross-correlation PIV. Section 2.1 presents a general description of 2D PIV, section 2.2 discusses the fundamentals of cross-correlation PIV, section 2.3 discusses sources of errors within PIV measurements, section 2.4 discusses calculations of differential and integral flow properties from PIV velocity data, section 2.5 discusses outlier identification methods and section 2.6 discusses advanced PIV methods. While PIV has become the dominant technique for flow field measurements, recent new methods have emerged that are allowing fluid mechanics experimentalists to interrogate and measure three-component velocities within a three-dimensional domain through time. One of these methods, the Three-Dimensional Defocusing Particle Image Velocimetry technique (3DDPIV) technique, will be presented in section 3.

# 2 TWO-DIMENSIONAL PARTICLE IMAGE VELOCIMETRY (2D PIV)

Particle Tracking Velocimetry (PTV), Laser Speckle Velocimetry (LSV), and Particle Image Velocimetry (PIV) all measure instantaneous flow fields by recording images of suspended seed particles in flows at successive instants in time. An important difference among the three techniques comes from the typical seeding densities that can be dealt with by each technique. PTV is appropriate with "low" seeding density experiments, PIV with "medium" seeding density and LSV with "high" seeding density.

Historically, LSV and PIV techniques have evolved separately from the PTV technique. In LSV and PIV, fluid velocity information at an "interrogation region" is obtained from many tracer particles, and it is obtained as the most probable statistical value. In PIV, a typical interrogation region may contain images of 10-20 particles. In LSV, the particle densities are so large that individual particles are not distinguishable. Consequently, the scattered light interfere to form speckles, hence its name Laser Speckle Velocimetry. Correlation of either particle images or particle speckles can be done using identical techniques. Hence, LSV and PIV are essentially the same technique, used with different seeding density of particles.

In PTV, the acquired data is a time sequence of individual tracer particles in the flow. In order to be able to track individual particles from frame to frame, the seeding density needs to be small. Unlike PIV, PTV results in sparse velocity vectors distributions. Guezennec, Y. G. *et al.*, for example, have developed an automated three-dimensional particle tracking velocimetry system that provides time-resolved measurements in a volume[3].

## 2.1 General Description of 2D PIV

### *2.1.1 2D PIV Setup*

The principle layout schematic of a modern 2D PIV system is shown in Figure 2.[4] First, the flow facility must be seeded with particles that act as fluid tracers (section 2.1.2). A pulsed light source (most often a laser) and its necessary optics used to generate a thin light sheet is used to illuminate a cross-section of the seeded flow field (sections 2.1.3 and 2.1.4). A camera located perpendicular to the light sheet is used to acquire global and sequential images of the illuminated flow field (section 2.1.5). Electronic equipment is used to generate and synchronize the laser pulsing with the camera's frame rate timing sequence (not shown), such that each image is singly exposed (section 2.1.5). Lastly, a data acquisition system (not shown) is used to record sequential images from the camera.

Generally speaking, particle displacements are locally calculated from the acquired images using a cross-correlation algorithm (sections 2.2, 2.3, 2.4, 2.5, 2.6). These displacements are then converted from the image pixelated domain to the spatial domain via a calibration procedure. Finally, the particle displacements within the spatial domain are then divided by the time separation between the laser pulses that singly exposed sequential images, i.e. velocity = displacement/Δt, to provide the velocity field.

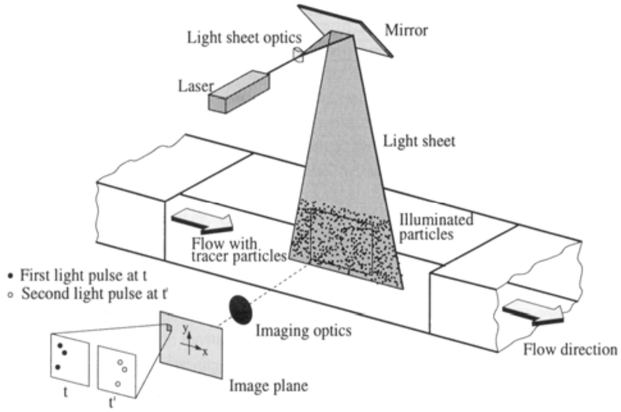

Figure 2: Principal layout of PIV system for typical wind or water tunnel applications[4]

### *2.1.2 Seeding Particles*

A PIV image is generated from the seeding particles in the flow field. Typically particles are added to the flow to have control over their size, distribution, and concentration. For ease of use, these particles should be non-toxic, non-corrosive, and chemically inert. They should also be small enough to be good flow tracers, yet large enough to scatter sufficient light for imaging. As a first estimate to particle motion in relation to fluid motion, it can be shown that the step response of the particle velocity, $U_p$, follows an exponential law[5]:

$$U_p(t) = U\left[1 - \exp\left(-\frac{t}{t_s}\right)\right], \tag{1}$$

where $t_s$ is the relaxation time of the particle,

$$t_s = d_p^2 \frac{\rho_p}{18\mu}, \tag{2}$$

where $\rho_p$ is the particle density, $d_p$ is the particle diameter, and $\mu$ is the fluid dynamic viscosity. Therefore, the smallest time scales of the fluid must be greater than the particle's relaxation time, if the particle is to accurately represent the local fluid velocity.

In a detailed review paper, Melling[6] presents a wide variety of tracer particles that have been used in liquid and gas PIV experiments, as well as methods of generating seeding particles and introducing them into the flow. For gas flow applications, theatrical smoke, different kinds of atomized oils, glass micro-balloons, titanium dioxide ($TiO_2$), and aluminum oxide ($Al_2O_3$) have been used. Typical theatrical smoke generators are inexpensive, and they generate plenty of particles. Oil can be atomized using devices such as a Laskin nozzle, generating particles in the micron to submicron range, which are particularly useful for high-speed applications. Titanium dioxide ($TiO_2$), and aluminum oxide ($Al_2O_3$) are useful for high temperature applications such as combustion, and flame measurements. For liquid flow applications, silver-coated hollow glass spheres, polymers, titanium dioxide ($TiO_2$), aluminum oxide ($Al_2O_3$), conifer pollen, and hydrogen and oxygen bubbles are typically used. Most liquid applications of PIV are in recirculating flow set-ups, so when concentrated particles in suspension are added to the flow, homogeneous seeding is achieved in a short time. Many gas applications are also in recirculating flow set-ups. However, for single pass-through systems, the task of achieving homogeneous seeding at the test section is not trivial, and typically requires upstream injection systems that can provide adequate mixing of the tracer particles before they arrive into the area of interest.

### *2.1.3 Light Sources*

In the point measurement technique of LDA, the coherence property of lasers is utilized to generate a fringe pattern at the measurement volume. For PIV, however, the laser's coherence property is not a requirement for measurements; hence, the lasers are used only as a source of bright illumination. In addition, PIV image acquisition should be acquired using short light pulses to prevent particle image streaking. Hence, pulsed lasers become obvious choices for PIV work. The most commonly used laser in modern PIV systems is the Nd:YAG laser. Nd:YAG lasers emit infrared radiation at 1064 nm, where for PIV applications, the frequency is doubled to 532nm, green, to allow for particle illumination and reflection in the visible spectrum. Presently, PIV Nd:YAG lasers can provide power from 12 mJ to 1000 mJ per pulse. Pulse durations for PIV Nd:YAG lasers are typically 5-10 nanoseconds, with pulse frequencies in the range of 1-1000 Hz, with power being inversely proportional to the pulse frequency. Pulse frequencies of 15 Hz and 30Hz are most commonly used in order to be able to properly synchronize with image acquisition cameras. As mentioned in section 2.1.1, cross-correlation PIV requires that each image be singly exposed. Therefore, to achieve a wide range of pulse separations, two separate laser cavities are used where the laser pulses can be adjusted with respect to each other using appropriate electronics equipment. These lasers, typically called dual lasers, are housed into a single unit, containing beam combining optics, frequency doubler, alignment optics, and an infrared beam dump. This setup allows the two laser pulses to be superimposed, and manipulated thereafter with the same optics (see Figure 3).

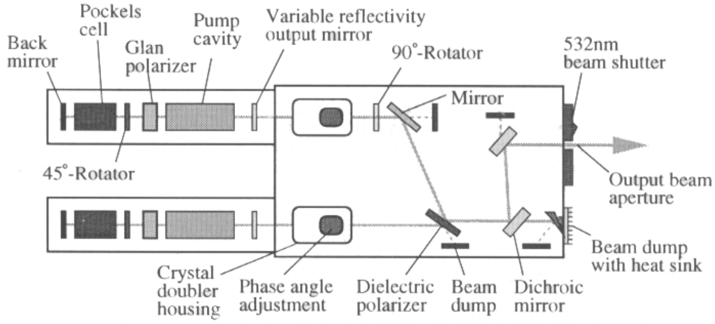

Figure 3: Dual-cavity Nd:YAG laser with resonators and beam combining optics[4]

### *2.1.4 Light Sheet Optics*

Fiber optics are commonly used for delivering Argon-Ion beams conveniently and safely. Single-mode polarization preserving fibers can be used for delivering up to 1 Watt of input power, whereas multi-mode fibers can accept up to 10 Watts.

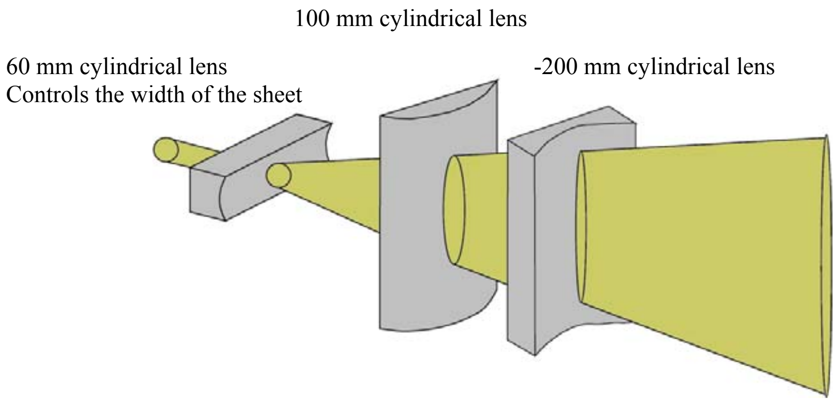

Figure 4: Example of a typical light sheet generating optical setup[7]

The short duration high power beams from pulsed Nd:YAG lasers can instantly damage optical fibers. Hence, the most standard methods generate a laser sheet by using laser optics. The variables to control in generating the light sheet in relation to the location of the laser with respect to the experimental setup are its spreading angle and its thickness, or its "beam waist". There are many ways to achieve proper control that include a variety of combinations of cylindrical and/or spherical lenses. A typical setup, for example as used by Maheo[7] employing 3 cylindrical lenses, is shown in Figure 4. In this example, the first lens is a diverging cylindrical lens that is used to spread the beam into a sheet. The second and third lenses are used to control the location of the beam's waist. To do this, second and third lenses, converging and diverging, respectively, and both rotated 90 degrees with respect to the first lens, are used. Then, varying the distance between the second and third lens will allow for the adjustment of the beam's waist's location.

### *2.1.5 Image Acquisition CCDs*

Cross-correlation cameras have become the preferred method of acquiring images. The cross-correlation cameras use high-performance progressive-scan frame interline CCD chips. Such chips include $m \times n$ light sensitive picture elements (pixels) and an equal number of storage cells (blind cells). The first laser pulse exposes the first frame, which is transferred from the light-sensitive cells to the storage cells immediately after the laser pulse (at the time of this publication, this transfer time can be as short as 200 ns). The second laser pulse is then fired to expose the second frame (see Figure 5). The storage cells now contain the first camera frame of the pair with information about the initial positions of seeding particles. The light-sensitive pixels contain the second camera frame, which has information on the final positions of the seeding particles. Using a framegrabber, these two image frames are then transferred sequentially from the camera onto the computer's RAM memory or its hard drive.

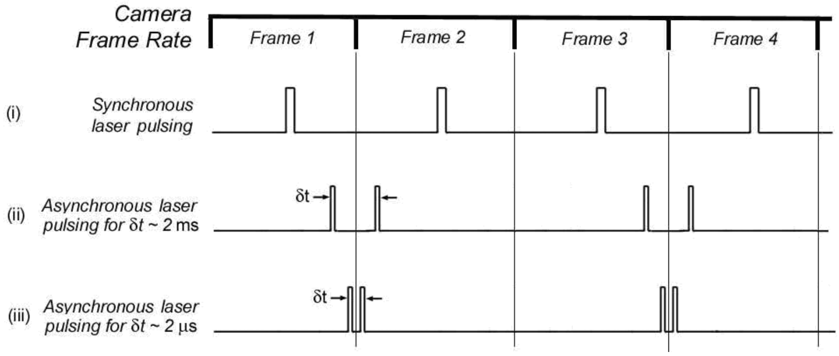

Figure 5: Timing diagram showing asynchronous laser pulsing in relation to the camera's frame rate[8]

Cross-correlation CCD cameras are available with resolutions up to 2672 x 4008 pixels, and framing rates from 4.85 Hz to as high as 1KHz, with the framing rate being inversely proportional to the resolution. 8-Bit digitization has been shown to be sufficient for most purposes[4]. Flow fields with velocities ranging from micrometers per second to supersonic speeds can be studied since inter-frame time separations down to few hundred nanoseconds can be obtained. One interesting option of these cameras is that they can be asynchronously reset. This is particularly useful in conjunction with the special triggering options for synchronizing measurements to external events, such as rotating machinery.

## 2.2 Fundamentals of Cross-Correlation Particle Image Velocimetry:

The historical development of PIV can be found in a series of papers archived in the SPIE Milestone Series Volume 99[9], which include many foundational and fundamental works including Willert & Gharib[10]; Adrian[11]; Lourenco. *et al.*[12]; Westerweel[13]). A fairly recent book, Particle Image Velocimetry – A Practical Guide, and paper by Westerweel, *Fundamentals of Digital Particle Image Velocimetry*[17], are also excellent sources of information on the fundamental aspects of PIV. Detailed derivations of the statistical description of cross-correlation PIV have been provided by Adrian[14,15,16], Westerweel[13,17], and Raffel *et al.*[4]. Below, the main results of these works are presented.

### *2.2.1 A Visual Representation of the Cross-Correlation Concept*

Visually, the correlation concept can be shown using Figure 6[8]. Figure 6a and Figure 6b show instantaneous images taken from a particle field at two consecutive times, with a time separation of Δt. If the second particle field is translated horizontally, superposition of the translated image with the first (Figure 6c) allows for visual detection of horizontal particle motions. Likewise, if the second particle field is rotated, superposition of the rotated image with the first (Figure 6d) allows for visual detection of rotating motions.

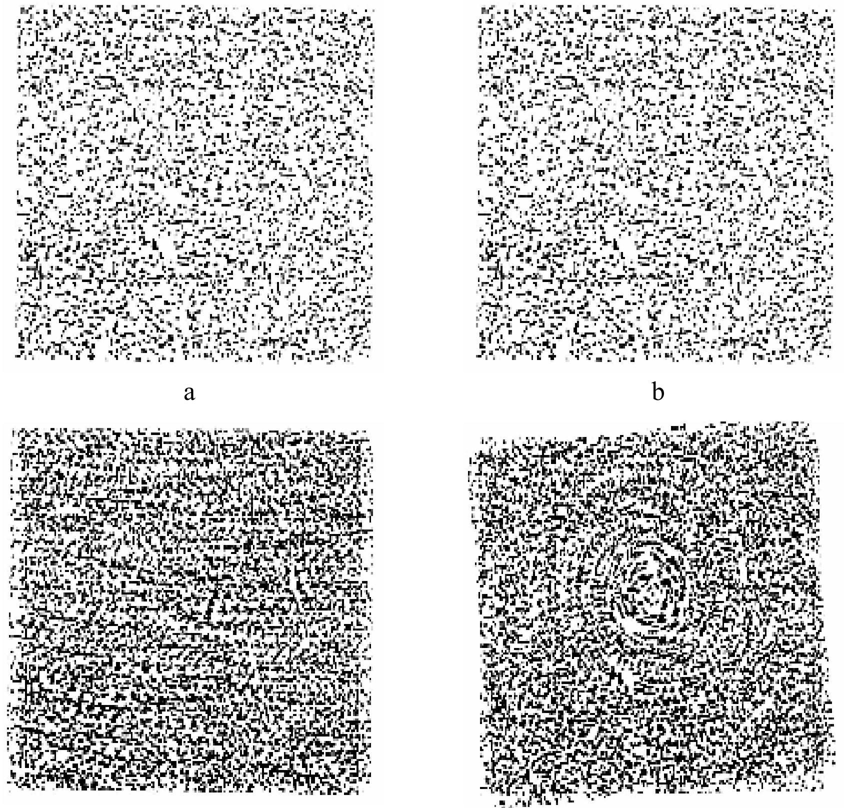

Figure 6: *a* and *b* are sample particle images. By translating a with respect to *b* and overlaying the two, a simulated translational shift is obtained and shown in *c*. By rotating *a* with respect to *b* and overlaying the two, a rotational shift is obtained and shown in *d*[8].

To obtain a quantitative two-dimensional vector field from such images, particle images must be systematically interrogated. To do so, these recorded images are sampled using an interrogation window (see Figure 7, left), the dimensions of which determine the spatial resolution of the measurement. The interrogation regions can be adjacent to each other, or more commonly, have partial overlap with their neighbors that will allow for increased spatial resolution. The shape of the interrogation regions can deviate from square to accommodate flow gradients.

Historically, two PIV methods have been developed, first an autocorrelation method was developed, which was then followed by a cross-correlation method. The auto-correlation method required that the images be doubly exposed, while the cross-correlation required that the images be singly exposed. The displacement information is then obtained once the correlation peak is determined using either of these methods. The autocorrelation analysis technique was developed for photography-based PIV, since it was not possible to advance the film fast enough between the two exposures. The auto-correlation function of a doubly-exposed image has a dominant central peak, and two symmetric side peaks. This poses two problems: (1) although the particle displacement is known, there is an ambiguity in the flow direction, (2) for very small displacements, the side peaks can partially overlap with the central peak, limiting the measurable velocity range. In order to overcome the directional ambiguity problem, image shifting techniques using rotating mirrors[18,19] and electro-optical techniques[18,19,20] have been developed. To leave enough room for the added image shift, larger interrogation regions are used for auto-correlation analysis. By displacing the second image at least as much as the largest negative displacement, the directional ambiguity is removed. This is analogous to frequency shifting in LDA systems to make them directionally sensitive.

Due to these complications and to the fact that dual-cavity lasers have allowed for very small pulse separations (see section 2.1.3), the preferred method in PIV presently is to singly expose images, and perform cross-correlation analysis, such as that as shown in Figure 7. First, image subsamples, *f(i,j)* and *g(i,j)*, are extracted at the same location within the images using an interrogation window (Figure 7a). Then, a cross-correlation procedure is performed on these two interrogated regions. Figure 7b shows an FFT cross-correlation algorithm, however, a direct cross-correlation procedure can also be used (see section 2.2.3). This procedure results in a cross-correlation distribution with the pixel domain within the interrogated regions with a dominant peak corresponding to the shift of the particles, (see Figure 7c and Figure 12) designated by *(dx,dy)*. Lastly, the pixel shift *(dx,dy)* is converted into a velocity through calibration parameters (see Figure 7d). Details of these steps from a theoretical foundation to practical implementation are described in the following sections.

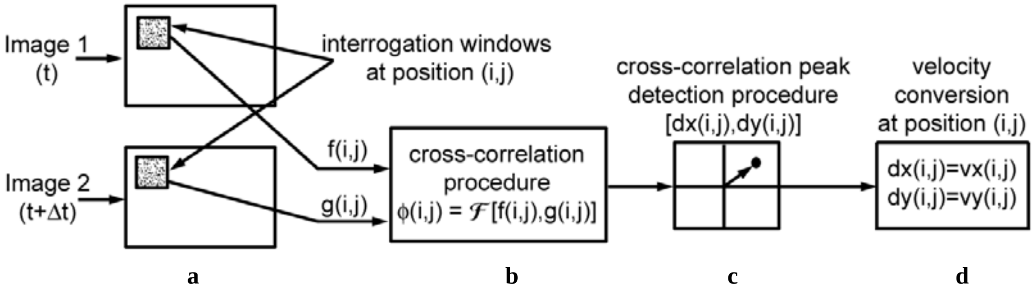

Figure 7: Cross-correlation data processing procedure using an FFT algorithm **a** an interrogation window subsamples the main sequential image pairs; **b** a cross-correlation procedure is performed, in this case, an FFT implementation is shown; **c** within the cross-correlation domain, the peak's location corresponding to the average shift of particles within the interrogation windows is identified; **d** this shift is converted to physical space, providing a velocity vector

### *2.2.2 Statistical Description of Cross-Correlation Particle Image Velocimetry[4,17]*

Before discussing the presently used cross-correlation analyses methods, it is important that a theoretical foundation is established. First, the tracer particle ensemble cross-covariance in physical three-dimensional space is presented. As these tracer particles are then imaged onto a two-dimensional domain, i.e. the CCD, the two-dimensional spatial ensemble cross-covariance of the projected tracer particles onto the two-dimensional domain is presented. Finally, several optimization considerations are discussed.

#### *2.2.2.1 Tracer Particle Ensemble Cross-Covariance in Physical Space*

The statistical description of fluid tracer particles is given by studying the ensemble of all possible tracer particle distributions, $G\left(\vec{X},t\right)$, for a given flow field, $u\left(\vec{X},t\right)$, where the tracer particle distribution within the physical spatial domain, $\vec{X}$, at time $t$ is defined to be

$$G\left(\vec{X},t\right)=\sum_{i=1}^{N}\delta\left[\vec{X}-\vec{X}_i\left(t\right)\right], \tag{3}$$

where $N$ is the total number of particles within the domain of interest, $\delta\left(\vec{X}\right)$ is the Dirac function, and $\vec{X}_i\left(t\right)$ is the position vector of the i-th particle at time $t$, so that the integral of $G$ over a volume yields the total number of particles within the volume. The particle distribution given in Equation 3 can also be represented in vector form as

$$\vec{\Gamma} = \begin{pmatrix} \vec{X}_1(t) \\ \vec{X}_2(t) \\ \vdots \\ \vec{X}_N(t) \end{pmatrix}. \tag{4}$$

In order to measure similarities between particle distributions at two different times, the ensemble cross-covariance is considered and defined as:

$$R_{G'G''}\left(\vec{X}', \vec{X}''\right) = \left\langle G'\left(\vec{X}'\right) G''\left(\vec{X}''\right) \right\rangle - \left\langle G'\left(\vec{X}'\right) \right\rangle \left\langle G''\left(\vec{X}''\right) \right\rangle, \tag{5}$$

where $\langle \cdot \rangle$ symbolizes the ensemble average. The ensemble mean of $G\left(\vec{X}\right)$ and $G'\left(\vec{X}'\right)G''\left(\vec{X}''\right)$ (suppressing the *t*-dependences, which are contained in *X*) are given by

$$\begin{gathered} \left\langle G\left(\vec{X}\right) \right\rangle = \int G\left(\vec{\Gamma}\right) \rho\left(\vec{\Gamma}\right) d\vec{\Gamma}, \\ \left\langle G'\left(\vec{X}'\right) G''\left(\vec{X}''\right) \right\rangle = \int\int G'\left(\vec{\Gamma}'\right) G''\left(\vec{\Gamma}''\right) \rho\left(\vec{\Gamma}' \middle| \vec{\Gamma}''\right) \rho\left(\vec{\Gamma}'\right) d\vec{\Gamma}' d\vec{\Gamma}'', \end{gathered} \tag{6}$$

where $\rho\left(\vec{\Gamma}\right)$ is the probability density function for $\vec{\Gamma}$, and $\rho\left(\vec{\Gamma}' \middle| \vec{\Gamma}''\right)$ is the conditional probability density function for $\vec{\Gamma}''$ given the initial state $\vec{\Gamma}'$. For a homogeneous tracer particle distribution, where the number density of the particles, *C*, is constant,

$$\begin{gathered} \left\langle G'\left(\vec{X}'\right) \right\rangle = \left\langle G''\left(\vec{X}''\right) \right\rangle = C, \\ \left\langle G'\left(\vec{X}'\right) G''\left(\vec{X}''\right) \right\rangle = C\delta\left[\vec{X}'' - \vec{X}' - \vec{D}\right] + C^2, \end{gathered} \tag{7}$$

where $\vec{D}\left(\vec{X}; t', t''\right)$ is the displacement of the tracer particle during the time interval $\left[t', t''\right]$. The ensemble cross-covariance thus reduces to

$$R_{G'G''}\left(\vec{X}', \vec{X}''\right) = C\delta\left[\vec{X}'' - \vec{X}' - \vec{D}\right]. \tag{8}$$

#### *2.2.2.2 Spatial Ensemble Cross-Covariance in Projected 2D domain*

It is important to realize that Equations 4 and 8 give the cross-covariance of particle distributions in the physical spatial domain, $\vec{X}$, thereby not making them directly applicable to images obtained from these particle distributions. Nevertheless, to develop a cross-covariance expression for PIV images, the imaging process must be first considered. As described in section 2.1.1, a laser sheet is generated, and used to illuminate a cross-section of the flow, which has been previously seeded with tracer particles. This light sheet will have a thickness, $\Delta Z_0$, typically with a Gaussian intensity profile within the depth of the sheet (see Figure 8). The laser sheet is assumed to be uniform in its plane, and the image acquisition optics are assumed to be aberration-free circular lenses with a given numerical aperture *F#*. The particles' images are assumed to be in focus, which is valid if the sheet thickness is less than the imaging depth of field.[11]

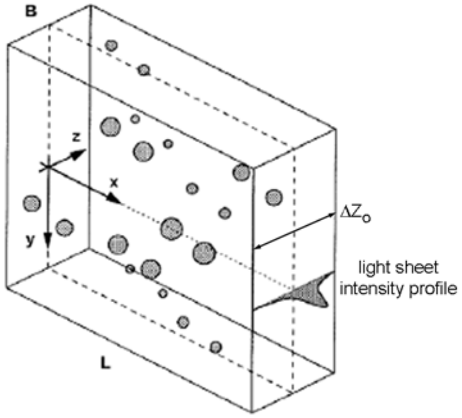

Figure 8: Three-dimensional volume representing the laser light sheet illumination and the particles illuminated within this light sheet[17]

The imaging process projects the particles' reflected illumination onto the planar image domain, $\vec{x} = (x, y)$, i.e. the CCD, and is represented mathematically as

$$g(\vec{x},t) = \frac{1}{I_z}\int I_0(Z)\,G(\vec{X},t)\,dZ\,, \tag{9}$$

where $x = MX$, $y = MY$, $M$ is the image magnification, and $I_0(Z)$ is the light sheet intensity profile with a maximum $I_z$, whereby it is assumed that tracer particle projections onto the image domain involves only an integration along the Z-coordinate. The tracer particles' image on the image domain can be represented by a point-spread function, *t(x,y)*, such that the image intensity *I(x,y)*, for particle tracer densities sufficiently low that do not allow particle overlap to occur, can be represented by

$$I(x, y) = I_z \int\int t(s - x, t - y)\, g(s,t)\, ds\, dt\,. \tag{10}$$

Using the definition given in Equation 5, the image ensemble cross-covariance, i.e. $I(\vec{x},t')$ and $I(\vec{x},t'')$, can be reduced to

$$R_{II}(\vec{s}) = F_0(\Delta Z)\cdot R_I \cdot \delta(\vec{s} - \vec{s}_D)\,, \tag{11}$$

where

$$R_I(\vec{s}) = C\Delta Z_0 M^{-2} I_Z^{\,2} t_0^{\,2} F_t(\vec{s})$$

$$t_0 = \iint t(x, y)\, dx\, dy$$

$$F_t(x, y) = \frac{1}{t_0^{\,2}}\iint t(u,v)\, t(u + x, u + y)\, du\, dv\,, \tag{12}$$

$$F_0(\Delta Z) = \frac{\int I_0(Z)\, I_0(Z + \Delta Z)\, dZ}{\int I_0^{\,2}(Z)\, dZ}$$

$\vec{s} = (x, y)$ and $\vec{s}_D = M\cdot(\Delta X, \Delta Y)$ is the particle tracer displacement on the image domain.[15] $F_0(\Delta Z)$ represents the loss of correlation due to tracer particles' motion perpendicular to the light sheet, $t_0^2$ is the normalization to $F_t$, the self-correlation of each tracer particle image, and $R_I$ is the image auto-correlation.

In implementation, ensemble averages of the flow field cannot be obtained unless the flow is steady or periodic. Therefore, if spatial averaging is ergodic with respect to ensemble averaging, the ensemble average can be replaced with spatial averaging defined as

$$C(\vec{s}) = \iint W'(\vec{x})\, I'(\vec{x})\, W''(\vec{x} + \vec{s})\, I''(\vec{x} + \vec{s})\, d\vec{s}\,. \tag{13}$$

Ergodicity can be established by considering the quantity:

$$\lim_{|\vec{r}|\to\infty} \frac{1}{|\vec{r}|}\int_{-|\vec{r}|}^{|\vec{r}|} \left| R_{G'G'}(\vec{X}, \vec{X} + \vec{r}) - \langle G'(\vec{X})\rangle^2 \right| d\vec{r}$$

A sufficient condition for ergodicity is that the above limit vanish. From (7) and (8),

$$R_{G'G''}(\vec{X}', \vec{X} + \vec{r}) = C\delta[\vec{r}]$$

$$\langle G'(\vec{X})\rangle = C$$

Since integration of the delta function in the first term in the integrand yields *C*, the concentration, the integrand vanishes identically and the ensemble average can be replaced with the spatial average as defined in (13). Since the distribution is homogeneous, this can be rewritten as:

$$C(\vec{s}) = \langle C(\vec{s})\rangle + C'(\vec{s}) = C'(\vec{s}) + R_D(\vec{s}) + R_C(\vec{s}) + R_F(\vec{s})\,, \tag{14}$$

where $\langle C(\vec{s})\rangle$ is the ensemble mean, $C'(\vec{s})$ is the fluctuating component with respect to the ensemble mean, $R_D(\vec{s})$ is the displacement correlation peak, $R_C(\vec{s})$ is the constant background correlation, and $R_F(\vec{s})$ is the correlation between the mean and fluctuating image intensities. These last two terms can be eliminated by subtracting the mean image intensity from *I'* and *I''*. The displacement correlation peak is given by

$$R_D\left(\vec{s}\right) = N_I F_I F_0 I_Z {t_0}^2 F_t * \delta\left(\vec{s} - \vec{s}_D\right), \tag{15}$$

where * denotes a convolution operation, $N_I = C\Delta Z_0 {D_I}^2 / M^2$ is the image density, $D_I^2$ is the area associated with the interrogation window, and

$$F_I\left(\vec{s}\right) = \frac{1}{{D_I}^2} \int W'\left(\vec{x}\right) W''\left(\vec{x} + \vec{s}\right) d\vec{s}\,. \tag{16}$$

It is important to realize that the spatial correlation resulting in Equation 15 correlates particles that are within two finite domains, *W'* and *W''*. As such, due to the flow, tracer particles can leave and enter these interrogation domains such that not all particles within the first interrogation domain, *W'*, will exist in the second interrogation domain, *W''*. The portion of the area coincident to both interrogation domains that contain images of the same tracer particles is denoted by Equation 16, and is pictorially shown in Figure 9. This term therefore represents the loss of correlation in the spatial cross-correlation (Equation 15) due to in-plane loss-of-pairs, and is the only difference between the ensemble correlation and the spatial correlation.

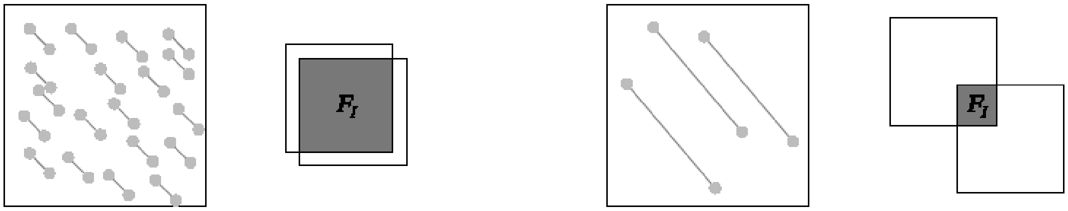

Figure 9: The number of particle–image pairs that can be contained in an interrogation region is reduced for increasing displacement[17]

*2.2.2.3 Optimization Considerations*

The spatial cross-correlation derived above is best suited for capturing translational motion. For such motions, the resulting cross-correlation produces a near delta-function peak within the cross-correlation domain. However, any deviation from translational motion, i.e. rotation and/or shear, causes a broadening of the peak distribution, as well as a reduction in its peak value. If the velocity differences (due to shear and/or rotation) within the interrogation volume are small with respect to the width of the interacting interrogation windows, then the displacement field will be sufficiently uniform.

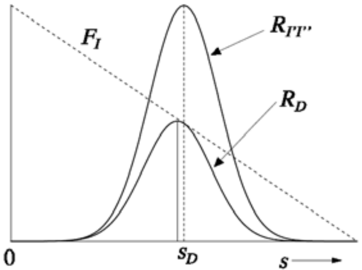

Figure 10: The displacement-correlation peak is skewed[17]. $R_{I'I''}$ represents tracer particle ensemble cross-covariance.

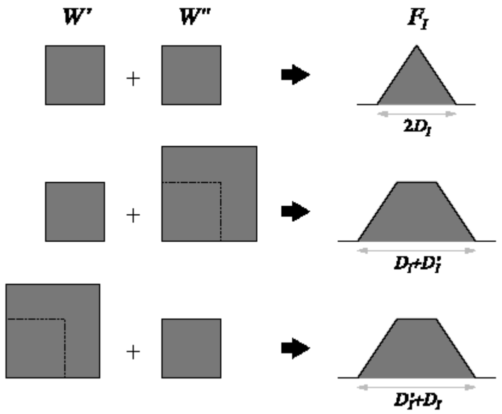

Figure 11: The effect of using differently sized interrogation windows on $F_I$[17].

While tracer particles' motion creates unpaired particle images within the two interrogation volumes that broaden the cross-correlation peak, it also shifts the peak value towards slightly lower displacement values (see Figure 10). This bias occurs for even the most basic motions, such as uniform flows, and is enhanced when flow gradients exist. Fortunately, there are three solutions that can eliminate this problem. The first is to divide the correlation by $F_I$[13]. The second is to use different size interrogation windows such that $F_I$ will be constant within its central portion, thus preventing any biasing[14]. This can be seen in the middle and bottom drawings of Figure 11. The third way is to shift one of the two interrogation windows an amount equal to the tracer particles' displacement, and in so doing, capture all tracer particle images common to both interrogation windows[21]. This can be seen in the top drawing of Figure 11, where the peak of $F_I$ would coincide with the cross-correlation peak.

To further ensure displacement measurement accuracy, it is important that the correlation peak, $R_D$, be strong with respect to the fluctuating correlation, $C'$ (see Equation 14). In this respect, $N_IF_IF_O$, which represents the effective tracer particle image pair density within the interrogation region, should be maximized. Keane and Adrian[14] suggest that for high intensity images

$$N_I F_I F_O > 7 \text{ and } F_I = F_O = 1, \tag{17a}$$

$$M\left|\Delta u\right|\Delta t / D_I < 0.03, \tag{17b}$$

$$M\left|\Delta u\right|\Delta t / d_\tau < 1, \tag{17c}$$

where $M$ is the image magnification, $\Delta u$ is the velocity difference within the interrogation window, $\Delta t$ is the time separation between image exposures, and $d_\tau$ is tracer particle image diameter. Following the procedures above, $F_I$ can be easily maximized to unity. Furthermore, Equations 17b,c provide constraints on the velocity gradients that can be tolerated within an interrogation window. Lastly, since $F_O$ (Equation 12) represents the loss of correlation due to tracer particles' motion perpendicular to the light sheet, it is important that out-of-plane tracer particles' displacements be less than one-quarter of $\Delta Z$.[17]

### *2.2.3 Digital Implementation of Cross-Correlation Particle Image Velocimetry*

Due to the nature of a CCD camera, once an image is acquired, it is pixilated and therefore discretized. The intensity value of each pixel is read through an analog-to-digital converter, and is therefore quantized; typically with an 8-bit converter for a total of 256 ($2^8$) quantized levels. The discretized cross-covariance can therefore be mathematically expressed within a discrete domain as[13,17]

$$C(r,s) = \frac{1}{M*N}\sum_{m=1}^{M}\sum_{n=1}^{N}\left[f(m,n)-\overline{f}\right]\left[g(m+r,n+s)-\overline{g}\right], \tag{18}$$

where $f(m,n)$ and $g(m,n)$ represent the first and second subsampled images, respectively, $M$ and $N$ represent the number of rows and columns within the images, $C(m,n)$ represents the discretized correlation function, *(r,s)* represents the location at which the correlation is calculated, and $\overline{f}$ and $\overline{g}$ represent the mean image intensity of the interrogation windows, *f* and *g*, respectively. Its corresponding in-plane loss-of-pair term is

$$F_I\left[r,s\right]=\left(1-\frac{|r|}{M}\right)\left(1-\frac{|s|}{N}\right),\text{[13,17]} \tag{19}$$

which, per section 2.2.2.3, can then be used to divide the cross-covariance (Equation 18) in order to obtain an unbiased displacement measurement. Willert[4,22] also suggests using another discretized cross-covariance description that inherently accounts for the in-plane loss-of-pair term:

$$\begin{aligned}
C\left(r,s\right) &= \frac{C_{II}\left(r,s\right)}{\sqrt{\sigma_I\left(r,s\right)}\sqrt{\sigma_{II}\left(r,s\right)}}\\
C_{II}\left(r,s\right) &= \sum_{m=1}^{M}\sum_{n=1}^{N}\left[f\left(m,n\right)-\overline{f}\right]\left[g\left(m+r,n+s\right)-\overline{g}\left(r,s\right)\right]\\
\sigma_I\left(r,s\right) &= \sum_{m=1}^{M}\sum_{n=1}^{N}\left[f\left(m,n\right)-\overline{f}\right]^2\\
\sigma_{II}\left(r,s\right) &= \sum_{m=1}^{M}\sum_{n=1}^{N}\left[g\left(m+r,n+s\right)-\overline{g}\left(r,s\right)\right]^2,
\end{aligned} \tag{20}$$

where $\overline{g}\left(r,s\right)$ is the average of $g$ coincident with the interrogation window, $f$.

To relieve the heavy computation burden, Willert and Gharib[10] have suggested using fast Fourier transforms (FFT) to significantly speed up the cross-correlation calculations, since doing so would reduce the number of computational operations for each interrogated region from $N^4$ to $N^2 log_2 N$. This procedure is outlined in Figure 7. Furthermore, computational efficiency can be further increased by using the symmetry properties of real-valued images, which state that the real part of an FFT is symmetric, while its imaginary part is anti-symmetric. Once the cross-correlation peak is determined, the interrogation window systematically interrogates the rest of the image pair, thereby providing a two-dimensional vector field.

### *2.2.4 Classical Sub-pixel Peak Finding Methods*

As the image domains are discretized, Equations 18 and 20 shows that the discretized cross-correlation domain will exist only at integer values (see Figure 12). This means that the peak value within the cross-correlation domain, corresponding to the particle shifts within the interrogated region, is at best measured to an integer value, with an uncertainty of ±1/2 pixel. While this may not seem significant, it is important to realize that, for example, for window sizes of 32 x 32, and maximum particle shifts of 1/3 of the window size, the uncertainty of a maximum particle shift of 10 pixels, is at best 5%. Given that vorticity and strain rates are differentiably calculated from the velocity (see section 2.3), their uncertainties will be about 10%, which is unacceptable. As such, methods were developed to obtain sub-pixel accuracy.

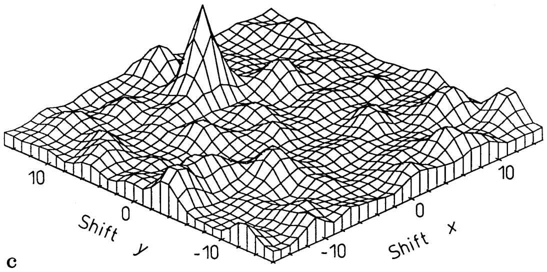

Figure 12: Sample cross-correlation peak showing single dominant peak corresponding to the magnitude and direction of particle shifts[10]

| Curve-Fitting Function | Three-Point Estimators |
|---|---|
| Peak Centroid<br>$f(x) = \dfrac{1^{st} \; order\ moment}{2^{nd} \; order\ moment}$ | $x_0 = \dfrac{(i-1)R_{(i-1,j)} + iR_{(i,j)} + (i+1)R_{(i+1,j)}}{R_{(i-1,j)} + R_{(i,j)} + R_{(i+1,j)}}$<br>$y_0 = \dfrac{(j-1)R_{(i,j-1)} + jR_{(i,j)} + (j+1)R_{(i,j+1)}}{R_{(i,j-1)} + R_{(i,j)} + R_{(i,j+1)}}$ |
| Parabolic<br>$f(x) = A(x_0 - x)^2 + B(x_0 - x) + C$ | $x_0 = \dfrac{R_{(i-1,j)} - R_{(i+1,j)}}{2R_{(i-1,j)} - 4R_{(i,j)} + 2R_{(i+1,j)}}$ $y_0 = \dfrac{R_{(i,j-1)} - R_{(i,j+1)}}{2R_{(i,j-1)} - 4R_{(i,j)} + 2R_{(i,j+1)}}$ |
| Gaussian<br>$f(x) = A\exp\left[\dfrac{-\left(x_0 - x\right)^2}{B}\right]$ | $x_0 = \dfrac{\ln R_{(i-1,j)} - \ln R_{(i+1,j)}}{2\ln R_{(i-1,j)} - 4\ln R_{(i,j)} + 2\ln R_{(i+1,j)}}$<br>$y_0 = \dfrac{\ln R_{(i,j-1)} - \ln R_{(i,j+1)}}{2\ln R_{(i,j-1)} - 4\ln R_{(i,j)} + 2\ln R_{(i,j+1)}}$ |

Table 1: Three-point estimators used to achieve subpixel resolution. The indices (*i,j*) correspond to the spatial location of the maximum location of the correlation value within the correlation domain. [4, 13]

Initially, centroiding, defined as the ratio of the first order moment to the zeroth order moment, was used, which required the correlation domain to be thresholded in order to define the region containing the correlation peak[23]. Unfortunately, this method strongly biased the displacement measurements towards integer values, creating a severe peak-locking effect on processed data (see Figure 13)[17,24]. Fortunately, more robust approaches were also developed, which curve-fitted the maximum peak and its two side-peaks, separately in both the x- and y-directions, with a function, in order to obtain sub-pixel accuracy. Typically, these three-point estimating curve-fits have been either parabolic or Gaussian, with Gaussian being the more frequently used (see Table 1) function. Its frequent use has been justified, since the particle images, well approximated by Gaussian intensity distributions, when correlated also result in a Gaussian intensity distribution. Its estimation is therefore much better predicted using a Gaussian curve fit, rather than a parabolic curve fit, which has been also been shown through calibration experiments.[25] Furthermore, its peak-locking effect (see section 2.3) is dramatically reduced (see Figure 13).

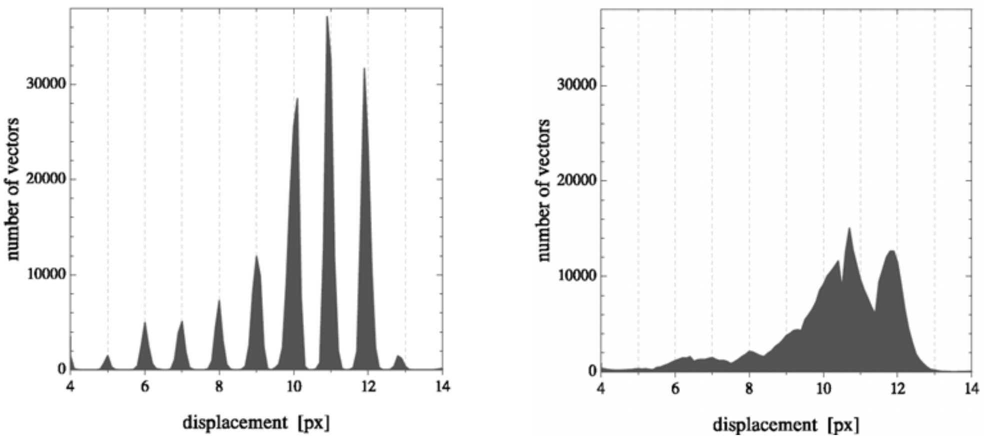

Centroid Peak Fit Gaussian Peak Fit

Figure 13: Histograms of the measured axial displacement (in pixels) in a turbulent pipe flow using the centroid and Gaussian peak fit for the sub-pixel interpolation. [17,24]

## 2.3 Sources of Error

As with all experimental methods, PIV measurements are susceptible to error. There are many parameters that affect the accuracy of PIV measurements: sub-pixel peak fitting, tracer particle image diameter, tracer particle image intensity distribution, window interrogation size, tracer particle image shift, quantization effects, background noise, displacement gradients within an interrogation window, and out-of-plane tracer particle motion. It is therefore important to be able to understand how each of these variables affects the error, or uncertainty of PIV measurements.

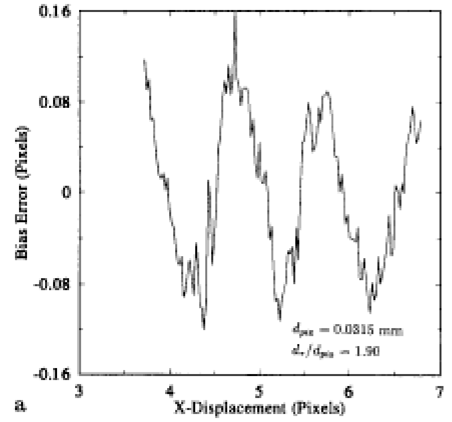

Figure 14: Bias error of horizontal displacements using 32 x 32 interrogation windows[26]

### 2.3.1 *Effect of Sub-pixel Peak Finding Methods*

Error analysis shows that the total error within a measurement can be expressed as the sum of systematic or bias errors, $\varepsilon_{biased}$, and random errors, which are usually characterized as root-mean-square values, $\varepsilon_{rms}$ :

$$\varepsilon_{total} = \varepsilon_{biased} + \varepsilon_{rms} \tag{21}$$

Using a photographic auto-correlation PIV system, Prasad *et al*.[26] have shown that for fixed tracer particle image size, a bias error did exist, and was due to the centroid sub-pixel peak finding method that was used (see Figure 14). Here, it can be clearly seen that the bias error is sinusoidal with respect to horizontal pixel shifts, where the bias error is zero at every integer and ½ integer pixel value.

In a detailed study of centroid, parabolic, Gaussian, and Whittaker (a truncated sinc kernel) interpolation peak finding methods, Lourenco & Krothapalli[25] have shown that the Gaussian and Whittaker's interpolation peak finding methods were the most superior in performance (see Figure 15).

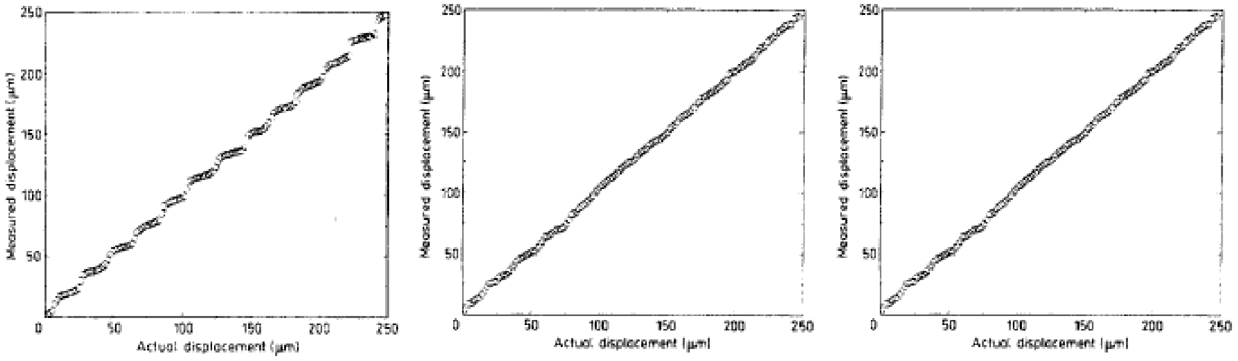

(a) (b) (c)

Figure 15: Actual vs. measured displacements for (a) Parabolic (b) Gaussian and (c) Whittaker's interpolation peak finding algorithms.[25]

In a further study, Roesgen[27] has suggested the use of the sinc function as a subpixel interpolation kernel, based on its spectral shape. The spectral shapes of various interpolation kernels are shown in Figure 16. In application to the data set that is periodic in the spectral domain, it can be seen that the nearest neighbor, linear, *M'4* (a kernel used to resample irregularly gridded data onto a regular grid), and Whittaker kernels are either too wide, causing spectral leakage from the side lobes of the data spectrum, or are not constant over the desired section of the data spectrum, causing filtering of the data. The spectrum of the sinc interpolation kernel, however, shows that it is uniform over the desired section of the data spectrum, avoiding any data filtration, and zero thereafter, preventing any spectral leakage from any of the data's spectral side lobes. This strongly suggests that the sinc function would be a good choice for an interpolation kernel.

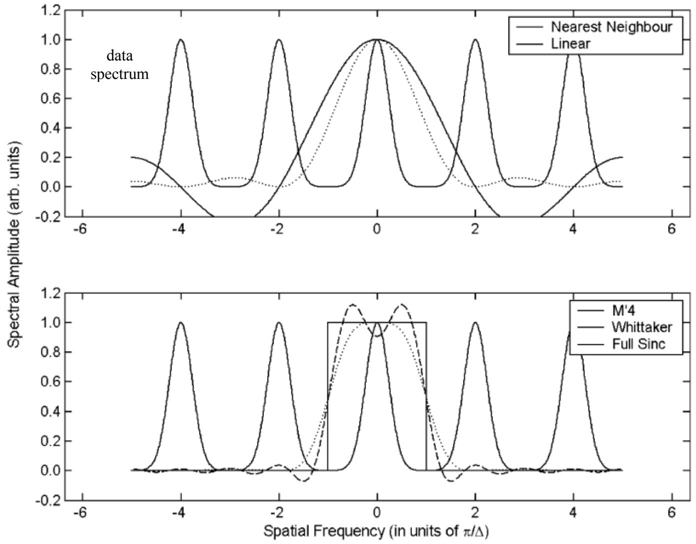

Figure 16: Spectral shape of different subpixel interpolation kernels[27]

Upon application to synthetic PIV images provided by the Visualization Society of Japan (http://www.vsj.or.jp/piv/), the interpolation error was plotted as a function of the sub-pixel shift (see Figure 17). It can be seen clearly that the sinc interpolation kernel has almost non-existent interpolation errors, easily surpassing the performance of the widely used Gaussian interpolation kernel.

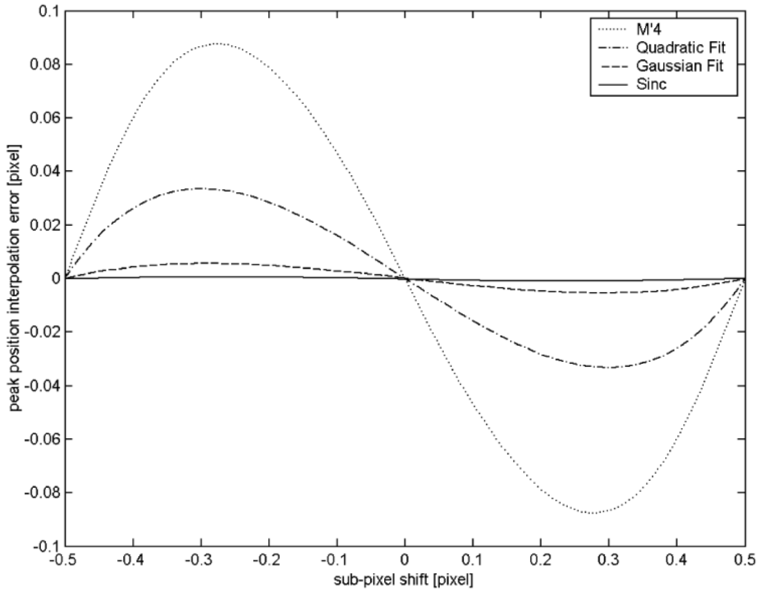

Figure 17: Subpixel interpolation error for different interpolation schemes[27]

Most recently, Nobach and Honkanen[28] have revisited subpixel interpolation kernels. Rather than implementing two one-dimensional interpolation kernels (one in the x-direction and one in the y-direction), they suggest using a two-dimensional 9-point Gaussian regression method (see Figure 18a-b). Their results as applied to particle images with and without noise are shown in Figure 19a-b. For the ideal case of images that are not noisy, the nine-point Gaussian regression and the two 3-point interpolators behave identically for particle image diameters larger than 4 pixels, since the particles are Gaussian shaped, and thus better approximated by the Gaussian one-dimensional and two-dimensional regression interpolators. For particle image diameters between 2-4 pixels, the extra particle image values used towards the two-dimensional regression are sufficiently different from a Gaussian regression that the introduced bias errors are non-negligible. Also discovered was that while the two-dimensional Gaussian regression worked perfectly for Gaussian shaped particle images or correlation peaks, if the particle shapes differed from the Gaussian shape, the regression did not work that well. To remedy this situation, the images were pre-processed with a low-pass Gaussian filter, which reduced the noise as well as deformed the particle shape towards a Gaussian profile. The results, also presented in Figure 19, show that for particle diameters just over 4 pixels, the bias error is reduced significantly to almost $10^{-4}$ pixels. Noisy images unfortunately reduce the performance of the filtered regression algorithm almost by an order of magnitude, though it still outperforms the two one-dimensional interpolation schemes for particle images larger than ~2.2 pixels (see Figure 19b).

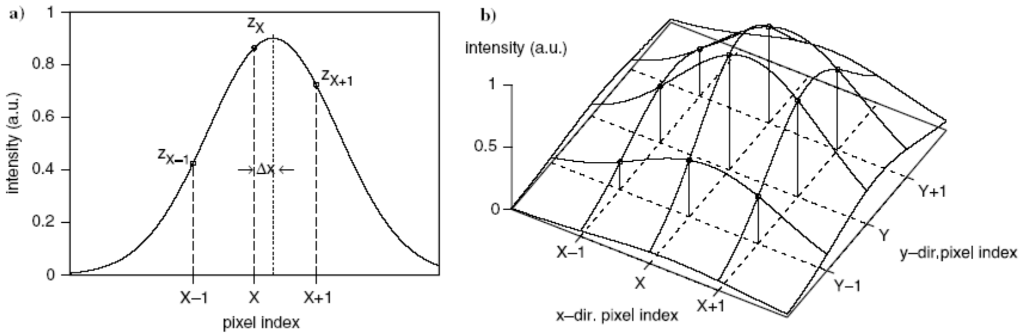

Figure 18: **a** One-dimensional three-point interpolation and **b** two-dimensional Gaussian regression[28]

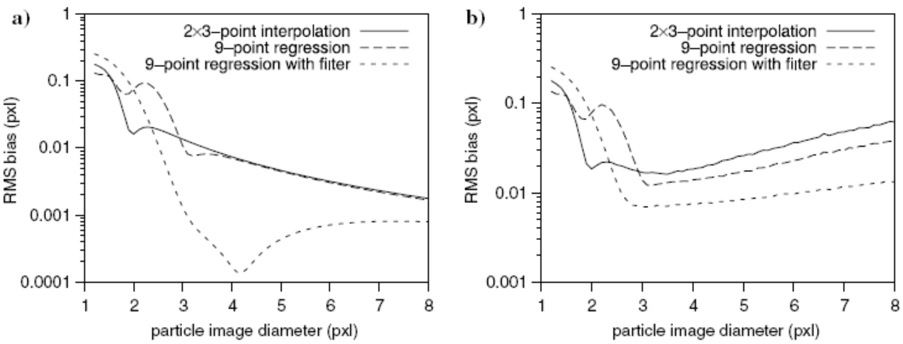

Figure 19: Root mean square (RMS) bias of the one-dimensional three-point interpolation and the two-dimensional Gaussian regression: **a** without noise and **b** with simulated photon noise[28]

### 2.3.2 *Effect of Tracer Particle Image Diameter*

Using Gaussian interpolation peak finding methods, Raffel *et al.*[4] performed Monte Carlo simulations of translational tracer particle shifts using different particle diameters and interrogation window sizes, in order to determine their effects on the measurement uncertainty. (see Figure 20). As is shown, the optimum tracer particle image diameter that minimizes the measurement uncertainty is just above 2 pixels, depending on the interrogation window size. It is also seen that larger window sizes further reduce the measurement uncertainty, as more particles within the interrogation window contribute to the cross-correlation peak.

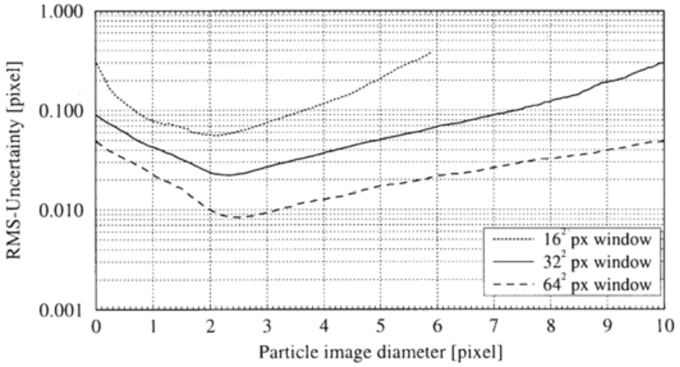

Figure 20: Measurement uncertainty (RMS random error) in digital cross-correlation PIV evaluation with respect to varying particle image diameter. (Simulation parameters: FFT-based correlations, quantization level = 8 bits/pixel, no noise, optimum exposure, top-hat light sheet profile, tracer particle image density=1/64 pixel$^{-1}$)[4]

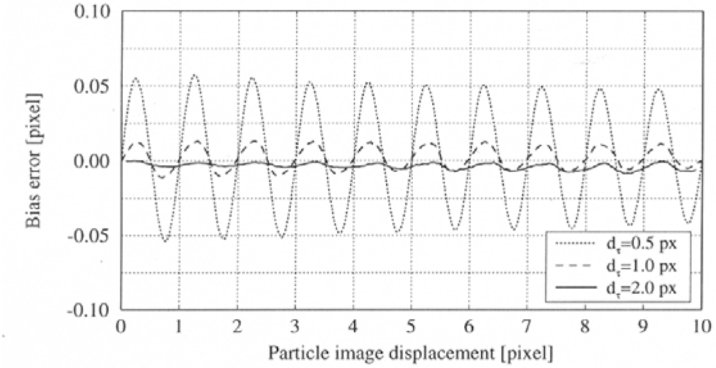

Figure 21: "Peak locking" is introduced when the particle image diameter is too small for the three-point estimator (simulation parameters identical to Figure 20)[4]

For particle image diameters smaller than the optimum diameter, the error increases, since the displacements become biased towards integer values (see Figure 21) that result in the "peak locking" effect introduced in the previous section. This indicates that the subpixel peak estimator, in this case the Gaussian peak finder, is not suitable for use with these tracer particle image diameters, since such particles are not Gaussian shaped. In fact, as can be seen from Figure 13, other peak finding methods, such as the centroid peak finder, can perform even worse.

### *2.3.3 Effect of Tracer Particle Image Shift*

In order to determine the effects of tracer particle image shifts, which had been predicted in section 2.2, Raffel *et al.*[4] performed Monte Carlo simulations (see Figure 22) of translational tracer particle shifts showing that for particle image shifts larger than 0.5 pixels, the measurement uncertainty grows linearly. For the same tracer particle image diameter, it can be seen that larger windows will result in a shallower slope since the larger window size will still capture more particles in common to both interrogated windows that are cross-correlated. The effect of the tracer particle image diameter can also be seen in Figure 22. Note that the 2 pixel tracer particle image diameter results show a much lower uncertainty, as well as a much shallower slope for tracer particle image shifts greater than 0.5 pixels, confirming the results shown in Figure 20. Also interesting is that for particle shifts less than 0.5 pixels, the measurement uncertainty is linear, reducing to zero at zero shifts.

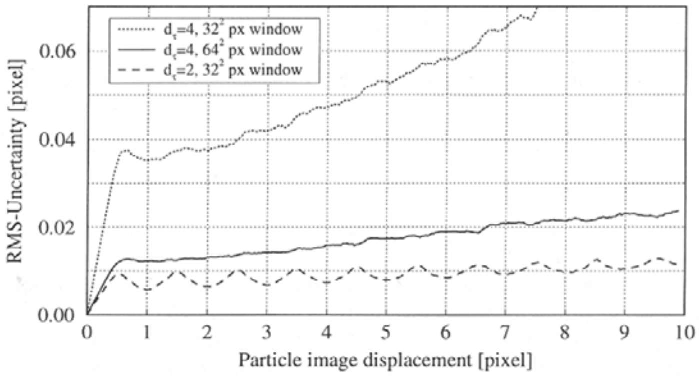

Figure 22: Monte Carlo simulation results using FFT-based correlations, for the measurement uncertainty in digital cross-correlation PIV evaluation as a function of particle image displacement[4]

As predicted in section 2.2.2.3, the bias errors that result due to smaller portions of the interrogation windows containing the same tracer particle images can be corrected by dividing the correlation by $F_I$[13]. This has also been tested by Raffel *et al.*, the results of which are shown in Figure 23.[4] It can be seen that the corrected results have substantially lower bias errors than the non-corrected results, thus verifying the predictions made by theory.

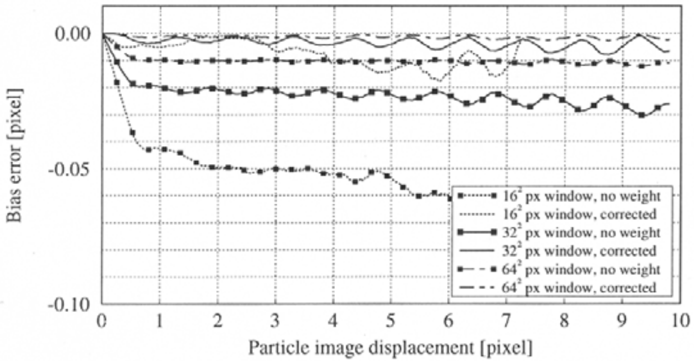

Figure 23: Simulation results showing the difference between actual and measured displacement as a function of the particle image displacement. Bias correction remove the displacement bias (simulation parameters: FFT-based correlations, $d_\tau$ = 2.0, no noise, top-hat intensity profile, tracer particle image density=1/64 pixel$^{-1}$)[4]

### *2.3.4 Effect of Tracer Particle Image Density*

As has been indicated previously, larger tracer particle densities will reduce the measurement uncertainty. This has also been specifically tested using Monte Carlo simulations of translational tracer particle shifts by Raffel *et al.*, the results of which are shown in Figure 24.[4] It can be clearly seen here that as the tracer particle image density increases from 5.2 to 32, the measurement uncertainty, for particle image shifts greater than 0.5, reduces by almost a factor of 3, from .04 to .015. As was also seen in Figure 22, for tracer particle image shifts less than 0.5 pixels, the measurement uncertainty is shown to be linear.

It should be noted, however, that the tracer particle density is not the only parameter that would determine a high probability of detecting a valid displacement. Other factors, such as the amount of in-plane displacement, $F_I$, and the amount of out-of-plane displacement, $F_I$,, also play a significant role, which has been expressed in Equation 17a. Towards this end, Raffel *et al*. have also performed Monte Carlo simulations showing what the percent valid detection probability is as a function of the effective particle image pair density, $N_I F_I F_0$, for a variety of tracer particle image densities, and interrogation window sizes (see Figure 25).[4] It is seen that for an effective particle image pair density greater than 7, the probability for detective valid displacements is greater than 95%. The theoretical Poisson distribution curves that describe the probability of detecting at least a given number of tracer particle image pairs, $P[n \geq i]$, is also shown. These theoretical curves show that detecting at least 3-4 particles matches the simulations, suggesting that in practice, the experimental setup and processing be optimized towards this end.

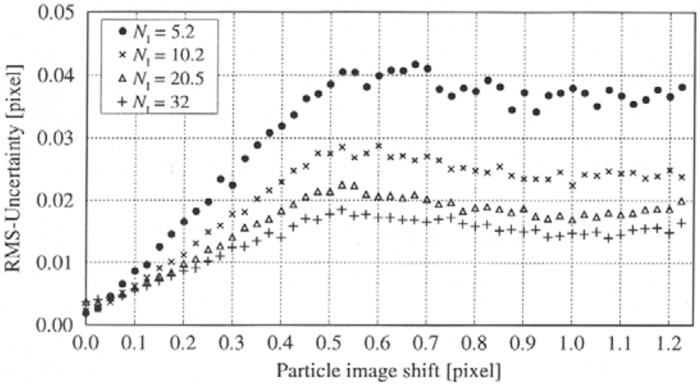

Figure 24: Measurement uncertainty for single exposure/double frame PIV as a function of particle image shift for various particle image densities $N_I$. (simulation parameters: FFT-based correlations, $d_\tau$=2.2 pixels, quantization level = 8 bits/pixel, 32 x 32 pixel interrogation window size, no noise, optimum exposure, top-hat light sheet profile.)[4]

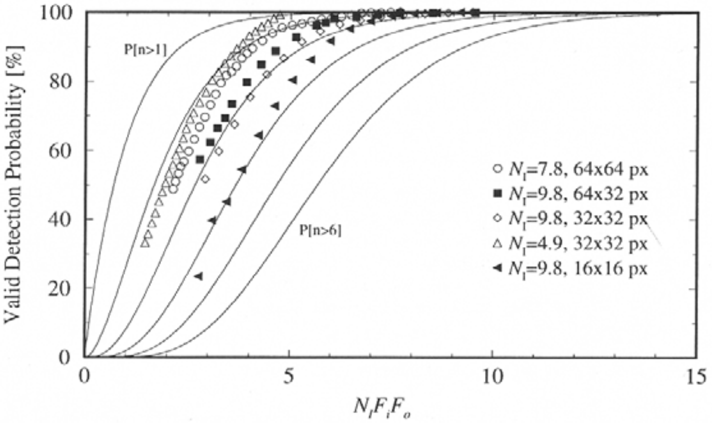

Figure 25: Vector detection probability as a function of the product of image density, $N_I$, in-plane loss of pairs, $F_i$, and out-of-plane loss of pairs, $F_0$. The solid line represents the probability for having at least a given number of particle images in the interrogation spot[4]

### *2.3.5 Effect of Tracer Image Quantization Levels*

Monte Carlo simulations of translational tracer particle shifts have been performed by Raffel *et al.* to determine the effect of image quantization levels on the measurement uncertainty (see Figure 26).[4] These results show that there is no difference in the measurement uncertainties for quantization levels of 4 bits/pixel and 8 bits/pixel for particle image shifts greater than 0.4 pixels. This implies that the noise due to the FFT-based correlation dominates. However, while it might be tempting to reduce image quantizations to 4 bits/pixel, it should be noted that the measurement uncertainty using 8-bit quantization drops by a factor of 3.5 as the particle image shift reduces to 0 pixels. As shown in section 2.3.3, by implementing the methods shown in section 2.2.2.3, it is possible to reduce the bias error to near zero values, suggesting that using 8-bit CCD will allow for further reduction of the measurement uncertainty. Any further reduction in quantization level below 4 bits/pixel is detrimental, as the measurement uncertainties increase by an order of magnitude.

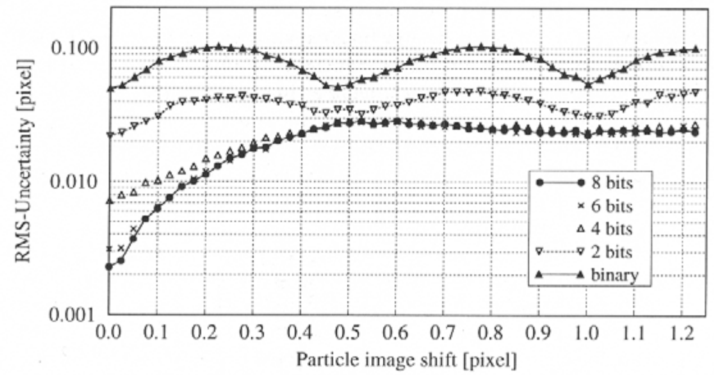

Figure 26: Measurement uncertainty for single exposure/double frame PIV as a function of displacement and image quantization (simulation parameters: FFT-based correlations, $d_\tau$=2.2 pixels, $N_I$=10.2, 32 x 32 pixel interrogation window size, no noise, optimum exposure, top-hat light sheet profile).[4]

### 2.3.6 *Effect of Background Noise*

Raffel *et al.* have also performed Monte Carlo simulations to determine the effect of background noise on the measurement uncertainty (see Figure 27).[4] The simulations used a white noise distribution added to each pixel, where the noise for each pixel was uncorrelated with its neighbors, or with its companion image at the same pixel location. These results show that for noise levels of up to 10%, the effect is negligible for particle image shifts greater than 0.4 pixels. However, there is noticeable change for particle shifts less than 0.4 pixels, thereby suggesting that low noise CCDs are desirable if the particle shifts can be reduced to less than 0.4 pixels (see sections 2.2.2.3 and 2.3.3).

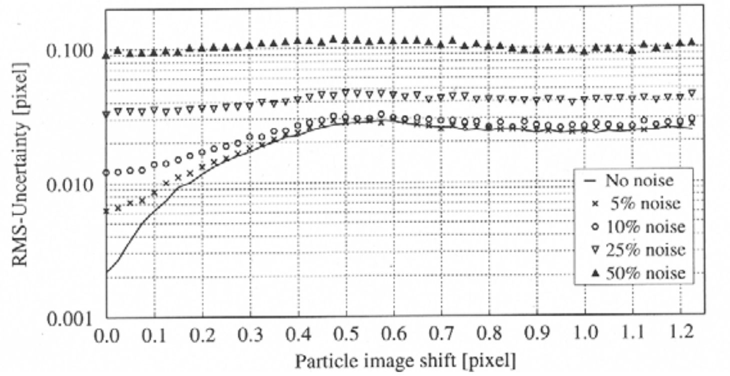

Figure 27: Measurement uncertainty as a function of displacement and various amounts of white background noise (simulation parameters: FFT-based correlations, $d_\tau$=2.2 pixels, $N_I$=10.2, 32 x 32 pixel interrogation window size, no noise, optimum exposure, top-hat light sheet profile).[4]

### 2.3.7 *Effect of Displacement Gradients*

Due to the fact that the pixels within most CCDs are either rectangular or square and therefore distributed in a Cartesian grid, the PIV methodology is best suited for measuring displacements that are uniform translations. However, since fluid flow, which PIV is designed to interrogate, is most often filled with velocity gradients, it is important to be able to characterize the behavior of PIV for tracer particles that contain gradients in their displacement fields. Raffel *et al.* have performed Monte Carlo simulations to determine the effect of displacement gradients on the measurement uncertainty, the results of which are shown in Figure 28.[4] Here, the particle image density and the interrogation window sizes were varied in order to ascertain their effects upon the measurement uncertainty for images with particle image shift gradients. Interestingly, it can be seen that the smaller interrogation windows and larger tracer particle image densities are able to tolerate larger displacement gradients. However, the window size seems to be the greater factor in reducing the measurement uncertainty since for the same interrogation window size, the measurement uncertainty reduction is relatively small compared to the its reduction when for the same particle image density, the window size is reduced.

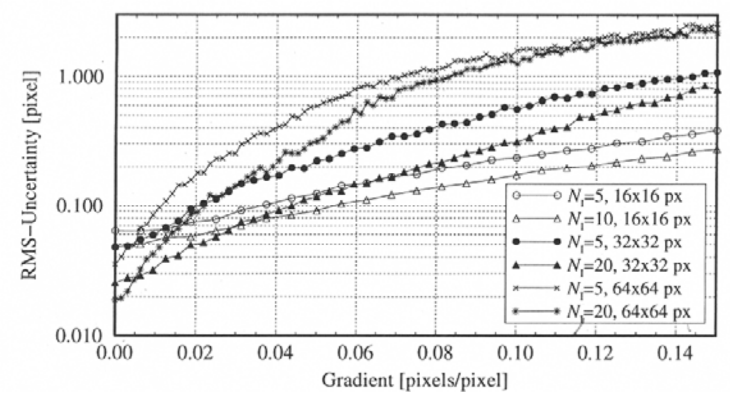

Figure 28: Measurement uncertainty as a function of displacement gradient for various particle image densities and interrogation window sizes (simulation parameters: FFT-based correlations, $d_\tau$=2.2 pixels, quantization level = 8 bits/pixel, no noise, optimum exposure, top-hat light sheet profile).[4]

## 2.4 Calculation of Differential and Integral Flow Properties from the Velocity field

In the formulations developed in the previous section, PIV provides global velocity data within a two-dimensional domain and does not directly measure important differentiable quantities, such as vorticity and strain rates, or integral quantities such as circulation, streamlines, or potential lines. As such, they must be post-calculated from the velocity fields. The following two sections discuss how such calculations can be achieved.

### *2.4.1 Calculation of Differential Flow Properties*

The vorticity and strain rates fields are both a consequence of the deformation tensor, which is:

$$\frac{d\vec{U}}{d\vec{X}} = \begin{bmatrix} \frac{du}{dx} & \frac{dv}{dx} & \frac{dw}{dx} \\ \frac{du}{dy} & \frac{dv}{dy} & \frac{dw}{dy} \\ \frac{du}{dz} & \frac{dv}{dz} & \frac{dw}{dz} \end{bmatrix}. \tag{21}$$

When using the vorticity vector, $\vec{\omega}$, and the strain tensor, $\vec{\varepsilon}$, the deformation tensor can be expressed as:

$$\frac{d\vec{U}}{d\vec{X}} = \begin{bmatrix} \varepsilon_{xx} & \frac{\varepsilon_{xy}}{2} & \frac{\varepsilon_{xz}}{2} \\ \frac{\varepsilon_{yx}}{2} & \varepsilon_{yy} & \frac{\varepsilon_{yz}}{2} \\ \frac{\varepsilon_{zx}}{2} & \frac{\varepsilon_{zy}}{2} & \varepsilon_{zz} \end{bmatrix} + \begin{bmatrix} 0 & \frac{\omega_z}{2} & -\frac{\omega_y}{2} \\ -\frac{\omega_z}{2} & 0 & \frac{\omega_x}{2} \\ \frac{\omega_y}{2} & -\frac{\omega_x}{2} & 0 \end{bmatrix}, \tag{22}$$

where $\varepsilon_{ij} = 1/2\left(\partial u_i/\partial x_j + \partial u_j/\partial x_i\right)$, and $\omega_i = \varepsilon_{ijk}\,\partial u_j/\partial x_k$. As 2D PIV is a two-dimensional technique that can only provide two-components of the velocity, the measurable deformation matrix reduces to

$$\frac{d\vec{U}}{d\vec{X}} = \begin{bmatrix} \varepsilon_{xx} & \frac{\varepsilon_{xy}}{2} \\ \frac{\varepsilon_{yx}}{2} & \varepsilon_{yy} \end{bmatrix} + \begin{bmatrix} 0 & \frac{\omega_z}{2} \\ -\frac{\omega_z}{2} & 0 \end{bmatrix}, \tag{23}$$

since the third velocity component, and $d/dz$ terms cannot be measured. Since the vorticity and strain rates fields cannot be directly measured, differentiation schemes must be used to derive these quantities. Such schemes, however, are susceptible to errors resulting from different grid spacing as well as noise within the velocity data. It is therefore important to be able to study and characterize various differentiation schemes in order to ascertain their performance.

| **Scheme** | **Implementation** | **Accuracy** | **Uncertainty** |
|---|---|---|---|
| Forward difference | $\left(\frac{df}{dx}\right)_{i+1/2} \approx \frac{f_{i+1} - f_i}{\Delta X}$ | $O(\Delta X)$ | $\approx 1.41\frac{\varepsilon_U}{\Delta X}$ |
| Backward difference | $\left(\frac{df}{dx}\right)_{i-1/2} \approx \frac{f_i - f_{i-1}}{\Delta X}$ | $O(\Delta X)$ | $\approx 1.41\frac{\varepsilon_U}{\Delta X}$ |
| Center difference | $\left(\frac{df}{dx}\right)_i \approx \frac{f_{i+1} - f_{i-1}}{2\Delta X}$ | $O(\Delta X^2)$ | $\approx 0.7\frac{\varepsilon_U}{\Delta X}$ |
| Richardson extrapolation | $\left(\frac{df}{dx}\right)_i \approx \frac{f_{i-2} - 8f_{i-1} + 8f_{i+1} - f_{i+2}}{12\Delta X}$ | $O(\Delta X^3)$ | $\approx 0.95\frac{\varepsilon_U}{\Delta X}$ |
| Least squares | $\left(\frac{df}{dx}\right)_i \approx \frac{2f_{i+2} + f_{i+1} - f_{i-1} - 2f_{i-2}}{10\Delta X}$ | $O(\Delta X^2)$ | $\approx 1.0\frac{\varepsilon_U}{\Delta X}$ |

Table 2: First order differential operators for data spaced at uniform *ΔX* intervals along the *X*-axis[4]

In a study of several differentiation schemes, Raffel *et al.*[4] were able to document estimates for the first derivative, *df/dx*, of a function *f(x)* at a discrete location, $f_i(x_i)$ (see Table 2). Here, $\varepsilon_U$ is the velocity measurement uncertainty. The accuracy of each scheme is defined as the truncation error associated with each scheme, and the uncertainty of each scheme is dependent on the velocity measurement uncertainty within the velocity field. Table 2 suggests that the forward and backward differentiation schemes would perform poorly, as both their accuracies and uncertainties are the highest.

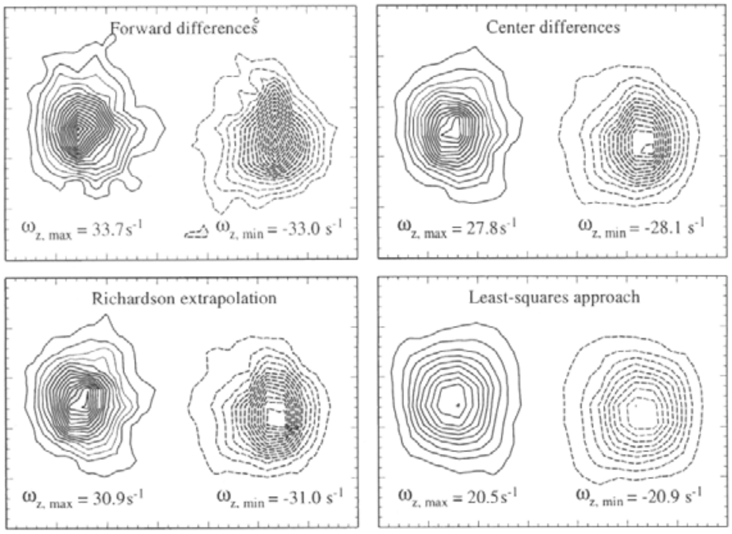

Figure 29: Vorticity field estimates obtained from twice oversampled PIV data, e.g. the interrogation window overlap is 50%. The vortex pair is known to be laminar and thus should have smooth vorticity contours.[4]

To test these predictions, these schemes were applied towards calculating the vorticity from the velocity field of a laminar vortex pair, where vorticity contours should be smooth.[4,29] Figure 29 shows the vorticity fields of the laminar vortex pairs resulting from various differentiation schemes. It can be clearly seen that the least-squares approach produces the smoothest vorticity contours. Interestingly, the Richardson scheme, which is designed to minimize truncation errors, shows not-so-smooth vorticity contours, suggesting that schemes that can best minimize both accuracy and uncertainty are the most desirable. An interesting observation is that while Table 2 suggests that the center differencing scheme should produce the best results since it best maximizes the accuracy while minimizing the uncertainty, it in fact does not perform as well as the least-squares scheme.

Also of interest is the effect of the grid spacing. Table 2 suggests that reducing the size of the grid spacing should decrease the accuracy, while increasing the uncertainty. By increasing the interrogation window from 50% (Figure 29) to 75% (Figure 30), the effects of the grid spacing size is seen. Overall, the results show the undesirable effect of an increased vorticity noise level. However, the peak vorticity value at the vortices' center is significantly increased, closer to its true value. This suggests that the finer grid spacing gives better estimates for the vorticity (though noisier), since the area over which the vorticity is averaged is smaller.

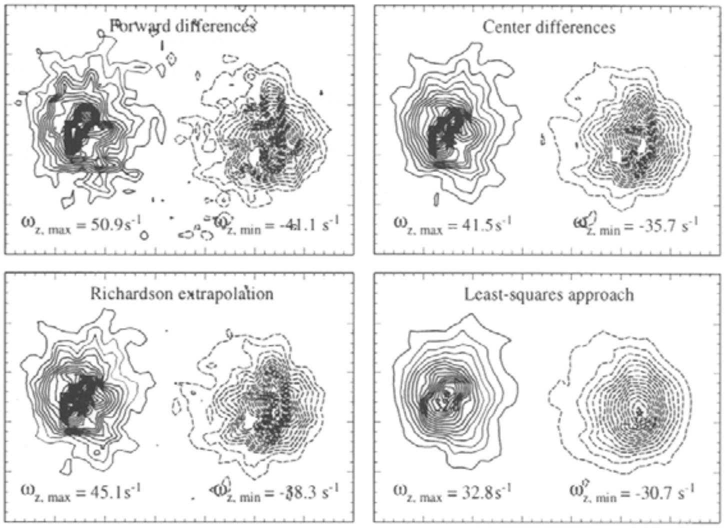

Figure 30: Vorticity field estimates obtained from four times oversampled PIV data, e.g. the interrogation window overlap is 75%.[4]

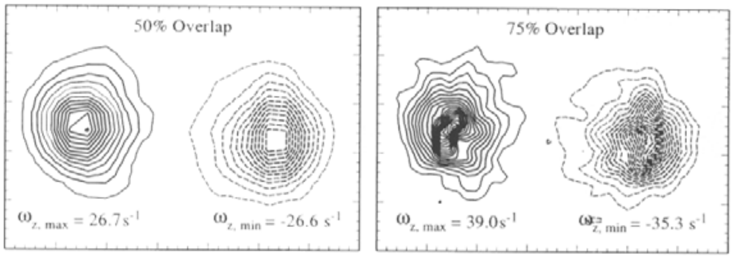

Figure 31: Vorticity field estimates obtained from PIV velocity fields by the circulation method: (left) the velocity field is twice oversampled, (right) four times oversampled. The contours of this laminar vortex pair are known to be smooth such that the nonuniformities are due to measurement noise.[4]

An alternative to calculating vorticity is through the use of circulation:

$$\Gamma = \oint_c \vec{u} \cdot d\vec{l} = \int \vec{\omega} \cdot d\vec{S} \tag{24}$$

where $\Gamma$ is the circulation, and $\vec{\omega}$ is the vorticity vector. Given the above, for two-dimensional flows, the average z-component vorticity can be calculated as

$$\overline{\omega}_z = \Gamma / A, \tag{25}$$

where $\overline{\omega}_z$ is the average z-component vorticity, and $A$ is the area over which the line and area integrals in Equation 24 are performed. This scheme is in fact identical to applying a 3 x 3 smoothing operator to the velocity field followed by a center differencing scheme.[13] This approach reduces the uncertainty to $\approx 0.61\,\varepsilon_U / \Delta X$.[4] The application of this scheme to the laminar vortex pair is shown in Figure 31. The vorticity contours shown are comparable to those shown for the least-squares scheme. However, the advantage of this approach is its better estimation of the peak vorticity value. Again, it can be seen that smaller grid sizes better estimate the value of the vorticity peaks, since the area over which the vorticity is averaged is smaller.

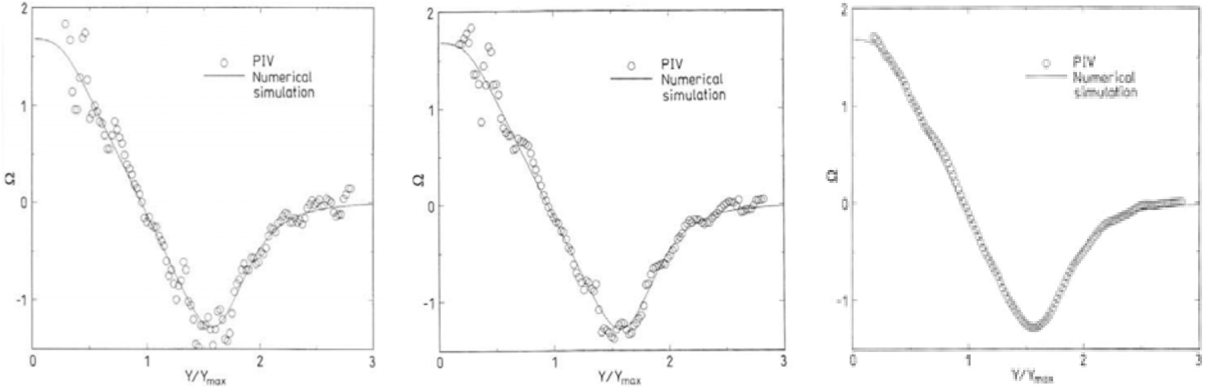

a b c

Figure 32a-c: **a** Wall-jet vorticity distribution (central-difference scheme); **b** Wall-jet vorticity distribution (Adaptive Scheme) **c** -jet vorticity distribution (adaptive scheme and least-squares) **[25]**

In an effort to further reduce the total error due to velocity uncertainties and truncation errors, Lourenco and Krothapalli[25] implemented an adaptive scheme based on the Richardson's extrapolation principle by combining the vorticity estimates at different grid sizes. Figure 32 shows a typical differentiation result using a central-difference scheme, while Figure 32b shows the improved result using the adaptive scheme. Further investigation showed that an improvement in accuracy could be achieved if each of the derivative estimates at the different grid sizes were computed using a least squares second order polynomial approximation (see Figure 32c).

Second order schemes have been further studied towards obtaining more accurate vorticity calculations. Fouras and Soria[30], recognizing that the vorticity error was composed of both a bias error and a random error, investigated the transmission of the velocity uncertainties into the vorticity random error, and the effect of grid spacing on the vorticity bias error using various implementations of a second-order polynomial $\chi^2$ fit, as described by Soria[31] that used different grid patterns for calculating the vorticity (see Figure 33).

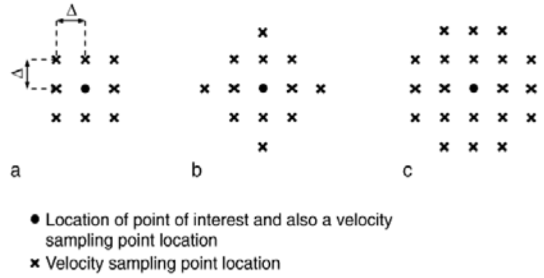

Figure 33a-c: Rectangular grid patterns used for the calculation of $\omega_z$ using the $\chi^2$ method. The locations of the velocity sampling points and the point of interest relative to the velocity sampling points are identified for. **a** The $\chi^2_9$ method which uses 9 velocity sampling points; **b** the $\chi^2_{13}$ method which uses 13 velocity sampling points and **c** the $\chi^2_{21}$ method which uses 21 velocity sampling points.[30]

In addition, they developed a theoretical analysis of the random error for the $\chi^2$ vorticity calculation method that estimates *a priori* the random vorticity error using $\chi^2_9$, $\chi^2_{13}$, and $\chi^2_{21}$ vorticity calculation method to be $\sigma_u/\Delta$, $.447\sigma_u/\Delta$, and $.328\sigma_u/\Delta$, respectively, where $\Delta$ is the grid spacing, and $\sigma_u$ is the velocity uncertainty. The results, shown in Figure 34, show that their theory predicts the numerical simulations quite well. Furthermore, it is seen that the random error transmission errors for the $\chi^2_{21}$ method is lower than the $\chi^2_9$ and $\chi^2_{13}$ methods by 67% and 26%, respectively.

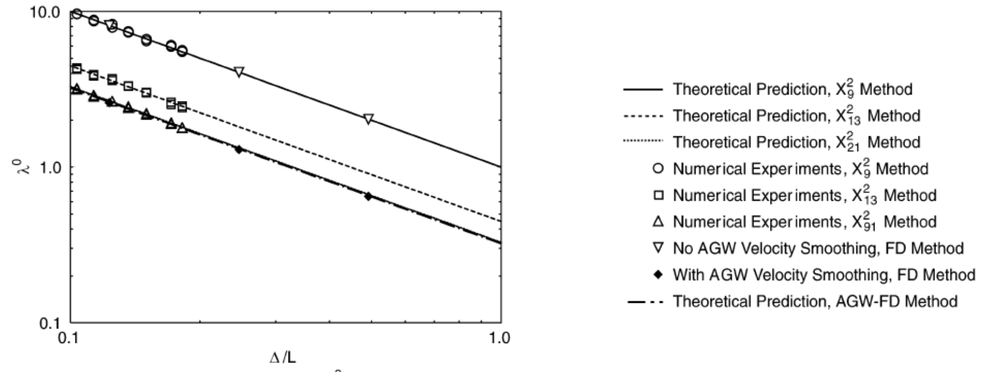

Figure 34: Ratio of normalized vorticity standard deviation to normalized velocity standard deviation, i.e. $\lambda_0$, as a function of $\Delta/L$. The solid lines are the theoretically predicted variations for vorticity calculated using the $\chi^2$ method. The symbols are the vorticity results calculated using the $\chi^2$ method from numerical experiments using noisy velocity data for the Oseen vortex flow field. Some corresponding results for vorticity calculated using the finite difference method without and with prior smoothing of the velocity field are also shown for comparison.[30] $\lambda_0 = \sigma^*(\omega_z)/\sigma^*(u)$, where $\sigma^*(\omega_z) = \sigma(\omega_z)/(V_{ref}/L)$, $\sigma^*(u) = \sigma(u)/V_{ref}$, $\sigma(\omega)$ is the random vorticity error, $\sigma(u)$ is the random velocity error, $L$ is a characteristic length scale of the flow, and $V_{ref}$ is a characteristic velocity of the flow.

The effects of grid spacing on the vorticity bias error were studied using numerical simulations of an Oseen vortex. The normalized vorticity bias errors as a function of normalized radial distance is shown in Figure 35. It can be seen that as the grid spacing gets smaller with respect to the characteristic length scale of the flow, the bias error reduces dramatically. While it is tempting to reduce this ratio to near zero values, it should be pointed out that in practice, this would require very highly resolved velocity measurements, which may be difficult to achieve with present technology. Also seen is that $\chi^2_9$ has much lower bias error than $\chi^2_{13}$ or $\chi^2_{21}$, which is due to the different spatial filtering characteristics of the vorticity calculation methods.

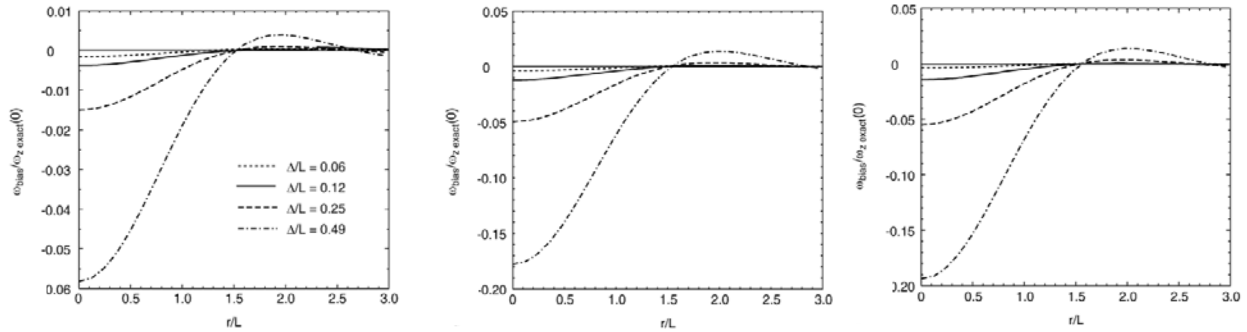

a b c

Figure 35: Bias error in $\omega_z$ calculation using exact discretized velocity data of the Oseen vortex for different $\Delta/L$ sampling separations and using different vorticity calculation methods. **a** $\chi^2$ method using 9 velocity sampling points, **b** $\chi^2$ method using 13 velocity sampling points and **c** $\chi^2$ method using 21 velocity sampling points.[30]

Recognizing that the spatial resolution is limited towards the large scales by the total image dimensions and towards the small scales by the interrogation window size, Foucaut and Stanislas[32] performed an exhaustive investigation of conventional schemes by studying their transfer functions. The differentiation schemes studied where 2nd, 4th, 6th, and 8th order centered difference, compact difference and Richardson's extrapolation schemes; 2nd, 4th, and 6th order noise minimized Richardson extrapolation schemes, a second-order noise minimized least squares scheme, and an eight-point circulation scheme. To characterize the PIV data, the PIV spectral response was first determined from experimentally obtained PIV results, and compared with results obtained with a hot wire anemometer (HWA).

Figure 36 shows the normalized vorticity bias errors as a function of the grid spacing with respect to the characteristic length scale of the flow, *Δ/L*. Comparison of this figure with Figure 34 shows that there is a conflict between simultaneously minimizing the random and bias errors: the larger the value of *Δ/L*, the lower the random vorticity error, but the higher the bias vorticity error, and visa versa. Overall, Fouras and Soria found that the $\chi^2_{21}$

vorticity calculation method resulted in the least overall error, thereby recommending it as the preferred differentiation scheme.

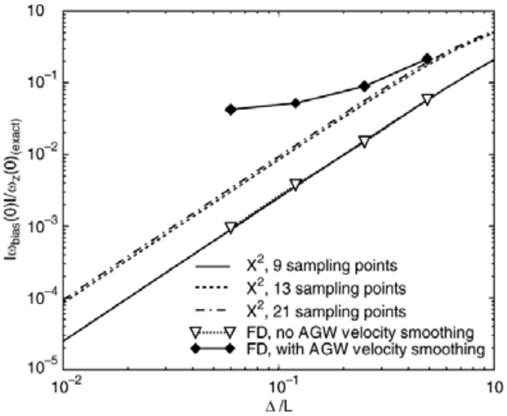

Figure 36: Bias error at the vortex centre, i.e. $|\omega_{\text{bias}}(0)|/\omega_z(0)_{\text{exact}}$ as a function of normalized velocity sampling distance $\Delta/L$ for the $\chi^2$ vorticity calculation method when 9, 13 and 21 velocity sampling points are used in the interpolation process and for the FD and AGW-FD vorticity calculation methods[30]

Also, a spectrum model,

$$E_{11PIV} = \left(E_{11HWA}^{1/2} + E_{noise}^{1/2}\right)^2 \left(\frac{\sin\left(kX/2\right)}{kX/2}\right)^2 \tag{26}$$

where $E_{noise}$ is the white noise level used to optimize the fit to the PIV spectrum ($E_{noise}$ varies with the inverse of the window size), $X$ is the interrogation window size, and $k$ is the wave number, was used to best fit and model the PIV spectrum. Furthermore, the window size was optimized by setting the cutoff wave number of the PIV spectrum to be where the signal-to-noise ratio was equal to 1. This approach resulted in a noise level on the order of 1% of the velocity dynamic range, an interrogation window size of 44 x 44 pixels$^2$, and a cutoff wave number of 1200 rad/m (see Figure 35).

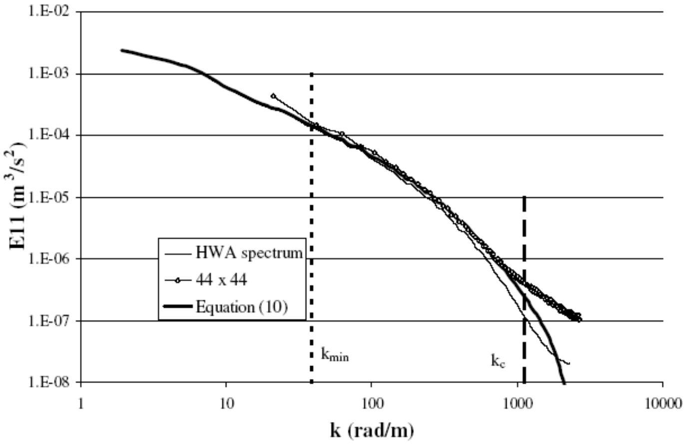

Figure 37: Power spectra of velocity along $x$, 44 × 44 interrogation window, frequency optimization. Equation 10 in the figure refers to Equation 26.[32]

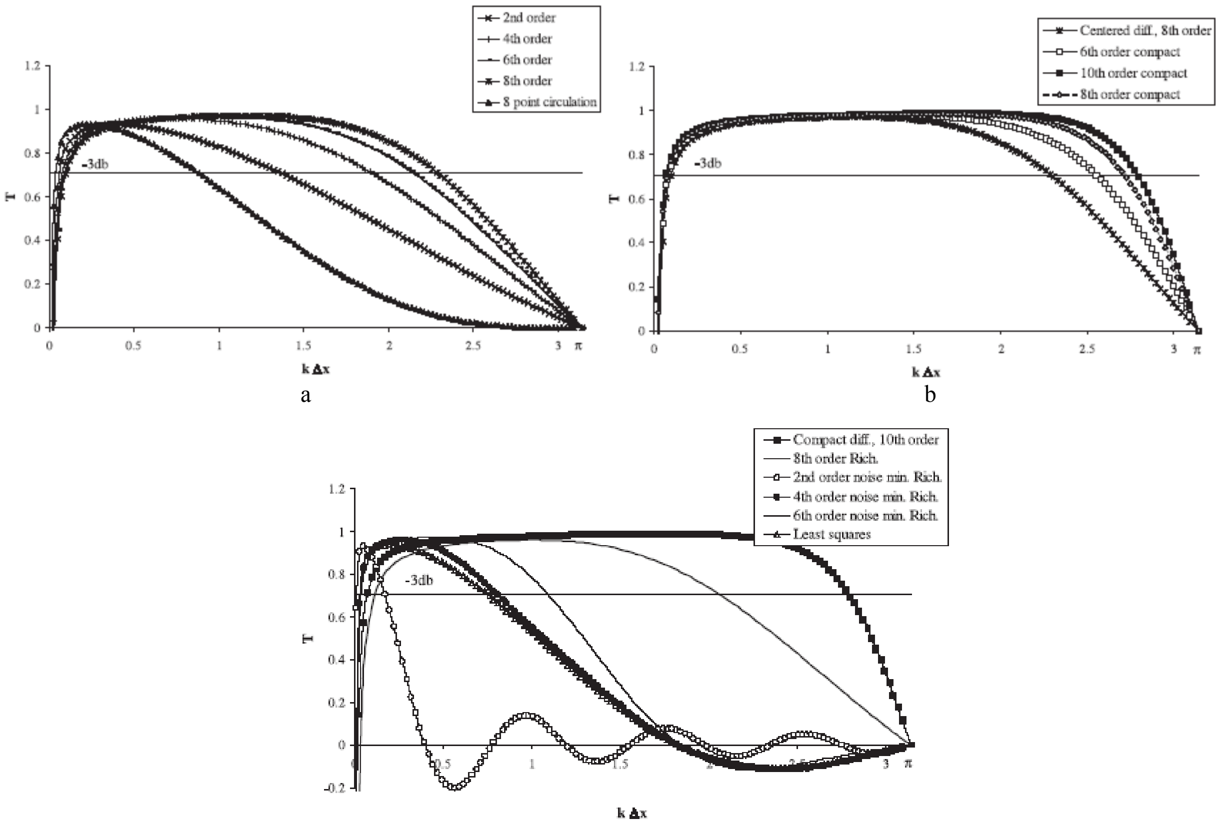

a

b

c

Figure 38: **a** Transfer functions of centered difference derivative filters. **b** Transfer functions of compact difference derivative filters. **c** Transfer functions of Richardson extrapolation derivative filters. [32]

The transfer functions of the differentiation schemes are shown in Figure 38a-c. Given that the cutoff wave number for the PIV data using 44 x 44 interrogation windows in these figures is 1.37, it can be seen that the differentiation scheme with the closest cutoff wave number is the second-order centered difference differentiation scheme, which has a cutoff wave number value of 1.39.

The power spectra of the differentiation schemes are shown in Figure 39. It can be seen that the best filter is the second-order centered difference scheme, since it has the same cutoff wave number as the PIV results. The 4th order Richardson extrapolation and the least-square schemes are identical in behavior, showing a strong filtering effect. On the other hand, the 6th and 10th order compact difference schemes have higher cutoff wave numbers, thereby amplifying any noise that would exist in the PIV data.

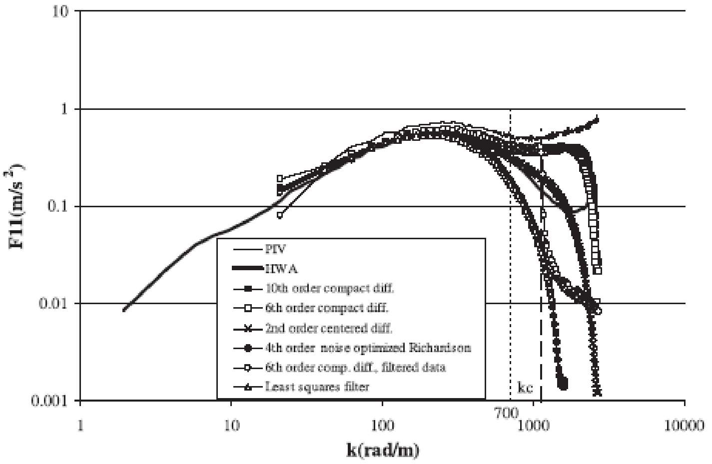

Figure 39: Power spectra of derivative of velocity along $x$, 44 × 44 interrogation windows. [32]

In an effort to overcome the conflict of simultaneously minimizing the random and bias errors, first pointed out by Fouras and Soria, and confirmed by Foucaut and Stanislas, Etebari and Vlachos[33] hypothesized that by combining the favorable bias-error reducing characteristics of the higher order implicit schemes with those of the noise-minimizing schemes, a new scheme could be developed that would reduce the overall errors and outperform the second order center differencing scheme recommended by both Fouras/Soria and Foucaut/Stanislas. Towards this end, they combined a 4th order compact scheme, which has low bias error, with a noise-optimized Richardson extrapolation scheme, which has low noise amplification, which uses a summation procedure of various spatial samplings of the derivatives. Their results suggest that this hybrid compact-Richardson extrapolation scheme provides nearly 30% less noise amplification while simultaneously reducing the bias error with respect to the centered difference scheme. They also suggest that further improvements might be attainable if the cutoff wave number of this scheme is adjusted to meet the characteristics of the particular experimental PIV data set.

### *2.4.2 Calculation of Integral Flow Properties[4]*

There are several parameters of interest that can be derived using integral methods. Circulation can be achieved using path integrals. Circulation is defined as

$$\Gamma = \oint_c \vec{u} \cdot d\vec{l} \ , \tag{27}$$

where $\vec{u}$ is the velocity vector, and $d\vec{l}$ is the differential path length of the total path defining the boundary *C*. The numerical integration of Equation 27 is straightforward using standard integration methods. Streamlines and potential lines can also be derived using integral methods. Assuming the flow is two-dimensional, the PIV results can be used to derive streamlines and potential lines using the following relations:

$$\Psi = \int_y u\,dy - \int_x v\,dx \,. \tag{28}$$

$$\Phi = \int_x u\,dx + \int_y v\,dy \,. \tag{29}$$

Performing the integration in Equation 28 to obtain S will not produce unique results, since different frames of reference will produce different streamlines. This is synonymous with reducing the Poisson equation

$$\nabla^2 \Psi = -\omega_z \tag{30}$$

into the Laplace equation

$$\nabla^2 \Psi = 0 \tag{31}$$

However, since the vorticity field is an approximation, and since boundary conditions need to be specified, this integration becomes difficult. Figure 40, for example, shows the different resulting set of streamlines that occur due to different choices of the frame of reference.

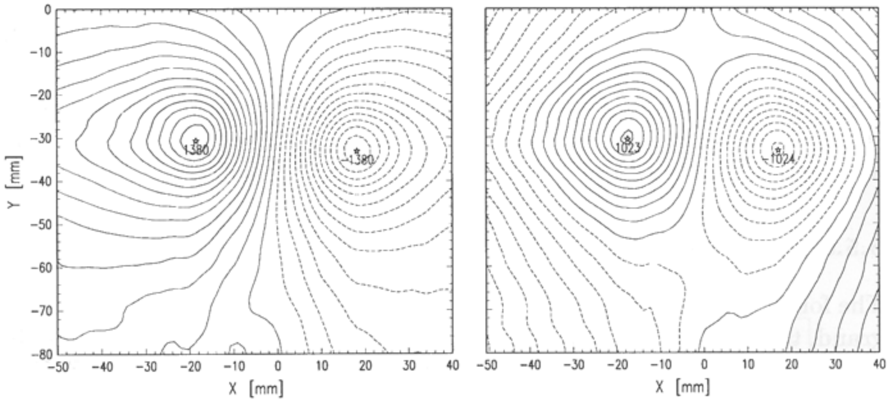

Figure 40: Two-dimensional stream function computed from vortex pair velocity data in a laboratory-fixed reference frame (left) and in a reference frame moving 20 mm/s upward with the vortex pair (right)[4]

## 2.5 Outlier Detection Methods

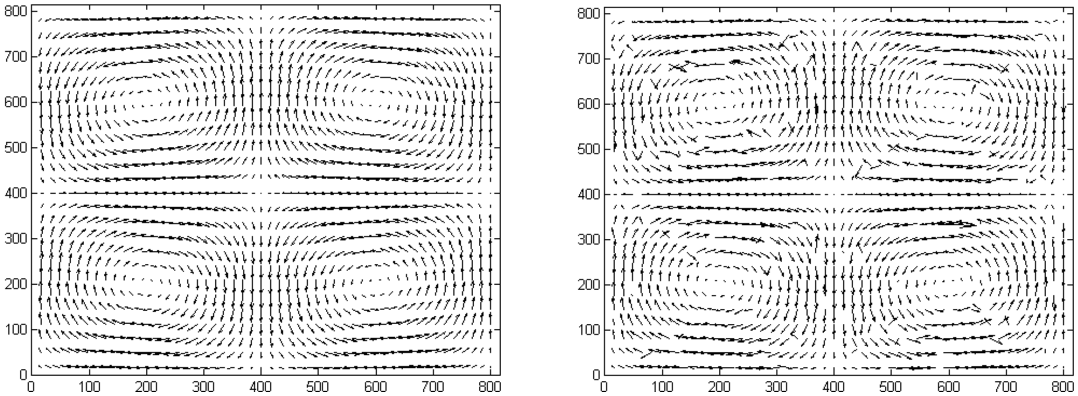

Figure 41: Example of a simulated vector field with outliers (left) shows the perfect simulated vector field; (right) shows the same field with outliers

Regardless of how well PIV images are acquired, the post-processing cross-correlation procedure can result in spurious vectors due to seeding inhomogeneities, effects of turbulence, varying intensity light sheet, etc. An example of spurious vectors that would infect an otherwise perfect velocity field is shown in Figure 41. Such outliers are most often visibly detectable, and are necessary to identify in order to maintain the integrity of the data to allow for proper data interpretation and derivation of differential and integral quantities, such as vorticity, strain rates, circulation, and streamlines (see section 2.4).

Westerweel[34] developed a statistical model for isotropic homogenous turbulent flow (in most cases flows that are not homogeneous or isotropic can be transformed to a domain where they are both) that characterizes outliers in PIV data. This model was then used to investigate three different outlier detection methods. For all these methods, a displacement residual vector was defined,

$$\vec{r}_{i,j} = \vec{V}'_{i,j} - \vec{V}_{i,j} \tag{32}$$

such that its magnitude squared

$$r^2_{i,j} = \left\| \vec{V}'_{i,j} - \vec{V}_{i,j} \right\|^2 \tag{33}$$

acts as the measure of the deviation of $\vec{V}'_{i,j}$, the vector in question, with respect to $\vec{V}_{i,j}$, the vector's true value. In practice, the true value of the vector is not known and is estimated using statistics, mean and variance, using the neighbors of the vector in question. The determination on whether the vector in question is spurious or not is then determined by statistical tests of the displacement residuals. In the first model, the global-mean test estimates the true value of the vector by using the mean velocity of the whole vector field. In the second model, the local-mean test estimates the true vector by using the mean velocity of a small neighborhood, typically a 3 x 3 eight-connected neighborhood (8 points), surrounding the vector in question. In the third model, the local-median test estimates the true vector components by using the median velocity components within a 3 x 3 neighborhood (9 points, including the vector of interest). Once an estimate of the true velocity is found, the displacement residuals are calculated, and tested against a user-selected threshold – if the displacement residual is larger than the threshold, the vector is labeled an outlier. Of the three methods, Westerweel found that the global-mean test performed the worst, the local-mean test better performed better, and the local-median performed the best. Specifically, the local-median test found 4 times fewer erroneous outlier vectors than the local-mean test. This procedure can be repeated until there is no change in the global vector field. While useful, this method is limited by the fact that the user must examine different threshold constants to determine the optimum value to use with a particular data set.

Raffel *et al.*[4] suggest a different version of the local-mean test. Rather than applying the test to the velocity magnitude, the test is applied to each of the velocity components. Then the average velocity of the eight points surrounding the vector in question is calculated:

$$\left\langle u_{i,j} \right\rangle = \frac{1}{N}\sum_{n=1}^{N} u(n) \tag{34}$$

where $N$ is the 8 neighboring points, $u_i(n)$ is velocity component, and <> denotes an average. Then the standard deviation is calculated:

$$\sigma_{i,j} = \sqrt{\frac{1}{N}\sum_{n=1}^{N}\left(\left\langle u_{i,j} \right\rangle - u(n)\right)^{2}}\ . \tag{35}$$

The residual is then tested against a threshold,

$$\left|\left\langle u_{i,j} \right\rangle - u(n)\right| < \varepsilon_{thresh}\ , \tag{36}$$

where

$$\varepsilon_{thresh} = C_1 + C_2\sigma_{i,j}\ , \tag{37}$$

and $C_1$ and $C_2$ are under-defined constants. This procedure can be repeated until there is no change in the global vector field. Similar to the local-median test, while useful, this method is also limited by the fact that the user must examine different constant values to determine the optimum values to use with a particular data set.

Nogueira *et al*[35] also describe a local validation method. First, the normalized velocity vector residual is calculated throughout the velocity domain,

$$\vec{r}_{i,j} = \frac{\sum_{n=1}^{N}\vec{V}_n - \vec{V}_0}{\sum_{n=1}^{N}\vec{V}_n} \tag{38}$$

where $N$ is the 8 neighboring points, $\vec{V}_n$ represents the 8 surrounding velocity vectors, and $\vec{V}_0$ is the velocity vector in question. The location within the velocity field where the residual is a minimum marks a zone where vectors achieve a degree of uniformity and hence a zone of "local coherence". Then, based on user-defined criteria, variations of vectors neighboring those labeled as coherent are examined and joined within the region of coherence. In this manner, regions of coherence grow and can merge. Then once an appreciable number of vectors are achieved within a zone, the vectors within this zone are validated. Figure 42(left) shows a PIV measurement field and Figure 42(right) shows the resulting validated vector field. Similar to the methods described above, this method is limited by the fact that the user must select two parameters, the tolerance of the prediction percentage, and the number of vectors a coherence zone should contain to be validated. The tolerance of the prediction percentage input, assumes *a priori* knowledge about the flow as to how much velocity differences can be tolerated. This value is typically set to 20%-35%. The number of vectors a coherence zone should contain for validation is around 10% of the total number of vectors for a correctly sampled flow.

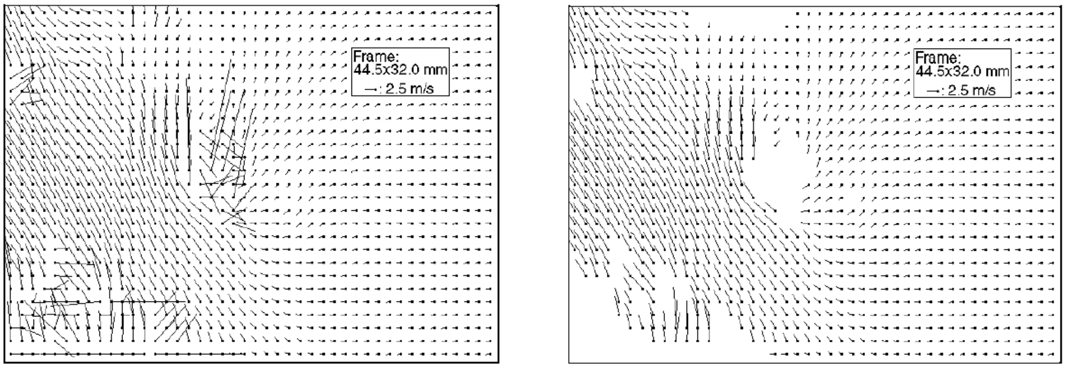

Figure 42: (left) Example of PIV measurement. Contains spurious vectors in an eddy, an undersampled mixing layer and a large random vector region due to light glimmer from the visualization window. (right) Validated data from left[35]

Song *et al.*[36] validate velocity vectors by verifying if the continuity equation is satisfied within Delaunay triangles. If all nodes within a triangle are good vectors, the total flux through all the sides of the triangle, $Q_1 + Q_2 + Q_3$, is very small. If a node within a triangle is an outlier, the total flux through the triangle is substantially larger. Hence, the normalized flux, which varies between 0 and 1 is defined as

$$E = \frac{Q_1 + Q_2 + Q_3}{\max\left(\left|Q^+\right|,\left|Q^-\right|\right)} \tag{39}$$

where $Q^+$ and $Q^-$ are the maximum positive and negative flux through the sides of the triangle, respectively. It is found that a threshold value of $E$=0.5 is sufficient to identify outliers. Figure 43(left) shows a simulated velocity field and Figure 43(right) shows the resulting validated vector field. It should be pointed out that while this is a robust method for outlier detection, the Delaunay Tessellation method was originally developed as a new PIV algorithm, and therefore should the user want to only use the outlier detection scheme, they must go through the added steps of generating the Delaunay triangles.

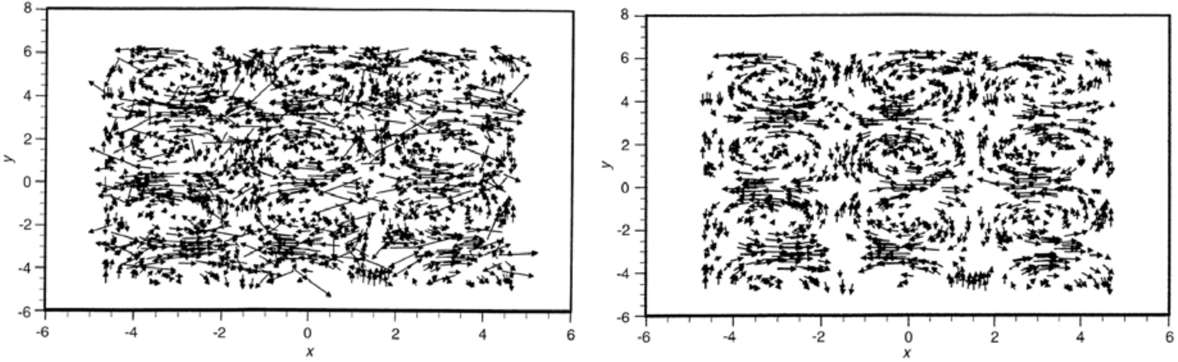

Figure 43: (left) Vector field by Delaunay Tessellation particle tracking Velocimetry method (DT-PTV) with 1505 particles (right) Vector field after removing the spurious vectors in the case of (left). Of the 1505 particles, DT-PTV found 1295 vectors. After removing the spurious vectors, 1077 vectors remained.[36]

Foucaut *et al.*[37] describe an iterative procedure for outlier detection. First, during the PIV procedure, the three highest peaks from the correlation domain are recorded, their corresponding residuals are calculated, and the best candidate is selected through the use of a local-median filter. This is done iteratively until there is no change in the global vector field. Second, the surviving residuals are thresholded to identify spurious vectors. As noted by the authors, the difficulty is in identifying the proper choice of the threshold. For this determination, the authors suggest estimating the percentage of valid vectors by hand in a few vector fields, and calculating the cumulative histogram of the residual normalized by the velocity vector located at a particular location. Then by selecting an appropriate percentage limit, the appropriate residual, and hence threshold, can be identified and implemented for the rest of the data set. Similar to previous methods, while useful, this method is also limited by the fact that the user must determine the optimum threshold by manually examining the cumulative histograms for selected flow fields.

Liang *et al.*[38] suggest that spurious vector detection is a pattern recognition problem, and as such, proposed to use cellular neural networks (CNN), a local feedback network, to identify outliers. The weights of the neurons are defined as

$$W_{i,j} = T - r_{i,j} \tag{40}$$

where $r_{ij}$, the velocity residual, is defined as

$$r_{i,} = \left| V_{x_i} - V_{x_j} \right| \quad or \quad r_{i,} = \left| V_{y_i} - V_{y_j} \right|, \tag{41}$$

depending on which of the velocity component field is being investigated, and $T$ is a threshold. The method was tested on several artificially generated stagnation flows scattered with spurious vectors, and which were also identified by the average velocity gradient defined as

$$G = \sqrt{\left[ \left( Vx_{i+1,j} - Vx_{i,j} \right)^2 + \left( Vx_{i,j+1} - Vx_{i,j} \right)^2 + \left( Vy_{i+1,j} - Vy_{i,j} \right)^2 + \left( Vy_{i,j+1} - Vy_{i,j} \right)^2 \right] \Big/ 2} \,. \tag{42}$$

Also, two parameters where introduced to evaluate the effectiveness of the methods. The first is the undetected rate defined as the ratio of the number of spurious vectors that are not detected over the total number of spurious vectors; the second is the over-detected rate defined as the ratio of the number of valid vectors that are detected as errors over the total number of spurious vectors. For comparison, their scheme was tested against the local-median test. The results suggest that the CNN outperforms the local-median test. Figure 44a shows that for the stagnation flow with $G = 0.2$, the threshold value that minimizes both the undetected and over-detected rates for the CNN and local-median filter are ~0.36 and ~0.47, respectively. However, the CNN percentage rate, ~0.08, is much lower than the local-median filter's percentage rate, ~0.2. Similarly, Figure 44b shows that for the stagnation flow with $G = 0.4$, the threshold value that minimizes both the undetected and over-detected rates for the CNN and local-median filter are ~0.6 and ~1.05, respectively. Again, the CNN percentage rate, near 0.0, is much lower than the local-median filter's percentage rate, ~0.53. Lastly, Figure 44c shows that for the stagnation flow with $G = 0.64$, the threshold value that minimizes both the undetected and over-detected rates for the CNN and local-median filter are ~0.85 and ~0.88, respectively. As in both previous cases, the CNN percentage rate, ~0.1, is much lower than the local-median filter's percentage rate, ~0.23. Also, similar to previous methods, while useful, this method is limited by the fact the user must select an appropriate threshold value. Nevertheless, as seen from the results, if the user picks thresholds slightly different than the optimum value, the increase in the undetected/over-detected percentages will be slight. For example, from Figure 44, it can be seen that if one uses the optimum threshold for $G$=0.2 (i.e. $T$=0.36 using the CNN method) on the $G$=0.4 and $G$=0.64 velocity fields, the over-detected percentage for both approaches infinity. Likewise, if one uses the optimum threshold for $G$=0.64 (i.e. $T$=0.88 using the CNN method) on the $G$=0.2 and $G$=0.4 velocity fields, the undetected percentage is 0.60% and 0.40%, respectively.

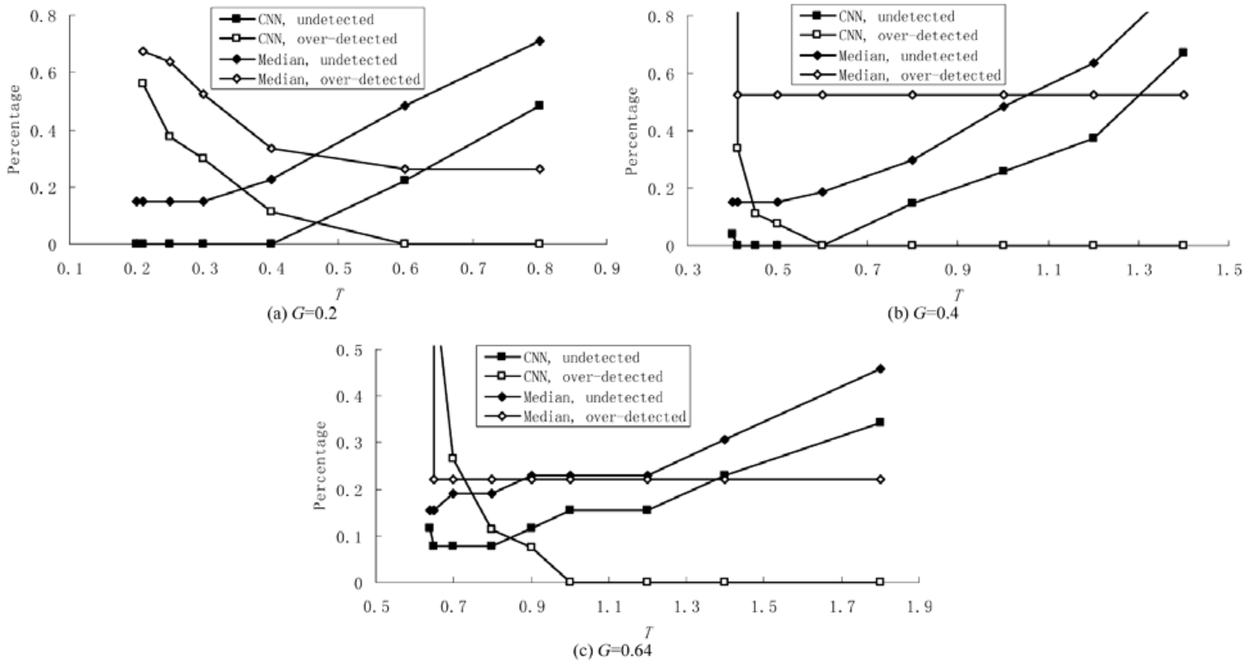

(a) $G$=0.2

(b) $G$=0.4

(c) $G$=0.64

Figure 44: Influence of the threshold on the detecting method, Error=10%. **a** G=0.2, **b** G=0.4, **c** G=0.64[38]

Shinneeb *et al.*[39], recognizing the importance of finding a threshold that is insensitive to flow gradients, suggested the use of a variable threshold procedure applied to both a local-median filter and the CNN procedure introduced by Liang *et al.*[38]. The procedure is as follows. First, an aggressive local-median filter is implemented to identify all outliers, even at the expense of falsely identifying good vectors as spurious vectors. The vectors are then replaced by a Gaussian-weighted average of their neighbors using Equation 43,

$$u_i = \frac{\sum_j \exp\left[-\frac{1}{2}\left(\frac{\left|\vec{x}_i - \vec{x}_j\right|}{H}\right)^2\right] u_j}{\sum_j \exp\left[-\frac{1}{2}\left(\frac{\left|\vec{x}_i - \vec{x}_j\right|}{H}\right)^2\right]}. \tag{43}$$

H = $4\sqrt{2}$ pixels and is the width of the Gaussian filter, and the summation is performed over a 5 x 5 region surrounding *i*. Next, a threshold field is defined by the mean deviation in each velocity component calculated from this newly generated velocity field

$$\tilde{T}_i'' = \frac{1}{N}\sum_{j=1}^{N}\left|u_i - u_j\right| + K, \tag{44}$$

where *K* is a constant and the summation is performed over the 8 neighboring points. This threshold field is then filtered by a Gaussian kernel (Equation 45)

$$T_i'' = \frac{\sum_j \exp\left[-\frac{1}{2}\left(\frac{\left|\vec{x}_i - \vec{x}_j\right|}{H}\right)^2\right] \tilde{T}_i''}{\sum_j \exp\left[-\frac{1}{2}\left(\frac{\left|\vec{x}_i - \vec{x}_j\right|}{H}\right)^2\right]}. \tag{45}$$

H = $4\sqrt{2}$ pixels and is the width of the Gaussian filter, and the summation is performed over a 9 x 9 region surrounding *i*.

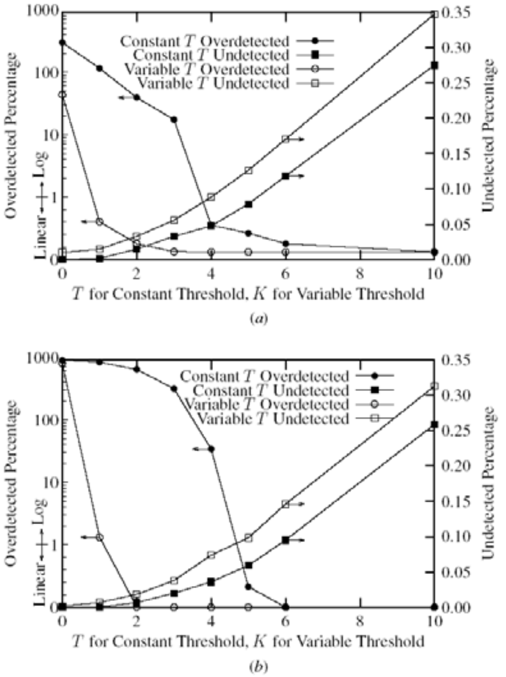

Figure 45: Performance of the **a** median and **b** CNN methods using uniform and variable thresholds for Field 1 (C=250 x $10^{-6}$) velocity field and 10% Type 1 spurious vectors[39]

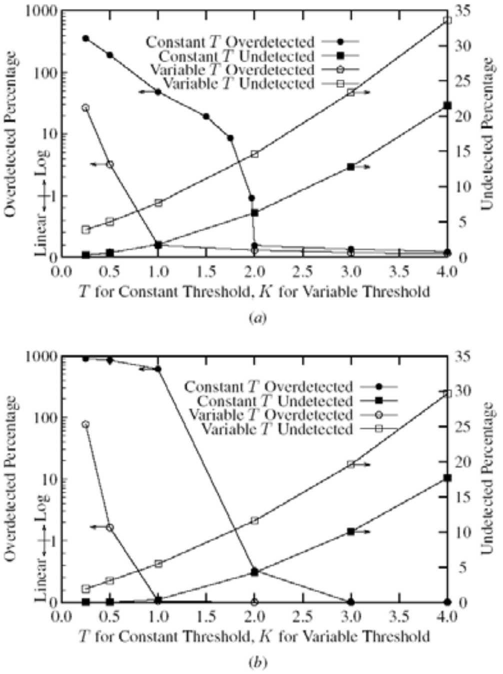

Figure 46: Performance of the **a** median and **b** CNN methods using uniform and variable thresholds for Field 2 velocity field ($N_x$=$N_y$=8, $V_{\max}$=10) and 10% Type 1 spurious vectors[39]

To test these procedures, two different types of flow fields were generated. The first field was described by

$$u = Cx^2 ; u = Cxy \, , \tag{46}$$

and the second was described by

$$\begin{aligned} u &= V_{\max} \cos\left( \frac{xN_x\pi}{L_x} + \frac{\pi}{2} \right) \cos\left( \frac{yN_y\pi}{L_y} \right) \\ v &= V_{\max} \sin\left( \frac{xN_x\pi}{L_x} + \frac{\pi}{2} \right) \sin\left( \frac{yN_y\pi}{L_y} \right) \end{aligned} \, , \tag{47}$$

where $C$ is a constant, $N_x$ and $N_y$ are the number of vortex cells in the $x$ and $y$ directions, respectively, $L_x$ and $L_y$ are the sizes of the particle images in the $x$ and $y$ directions, respectively, and $V_{\max}$ is the maximum velocity component. In addition, two different types of spurious vectors were used to populate these flow fields. The first type calculates a spurious vector in a random direction and magnitude distributed uniformly between zero and the maximum velocity within the velocity field. Such a spurious vector is designed to simulate the identification of a noise peak within the correlation domain far removed from the signal peak. The second type calculates a spurious vector whose magnitude deviates by a specified percent of the correct local velocity; its direction is randomly chosen. Furthermore, to simulate seeding imperfections, these outliers were positioned in randomly located clusters. To test the performance of this approach, the undetected and over-detected definitions introduced by Liang *et al.*[38] were used. From the results shown in Figure 45 and Figure 46, it can be seen that both the median and CNN methods, using a variable threshold, outperform the constant threshold method. Also of interest was the variability of the optimum threshold with respect to flow fields having varying velocity gradients. The results, shown in Figure 47, show that these optimum variable thresholds are much more constant with respect to varying velocity gradients, indicated by $C$, than the optimum constant threshold. Results for Field 2 show similar results. Lastly, it should be pointed out that the smoothing filter parameter, $H$, has an impact on the percentage of over-detected vectors (see Figure 48). This is due to the fact that it is a function of the interrogation resolution and also the experimental conditions.

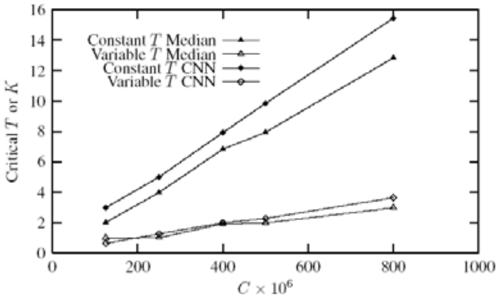

Figure 47: Critical value of $T$ and $K$ for constant and variable techniques. The critical value of $T$ or $K$ is determined as that value which yields 1% over-detected vectors. These results are for Field 1 velocity fields and 10% Type 1 spurious vectors.[39]

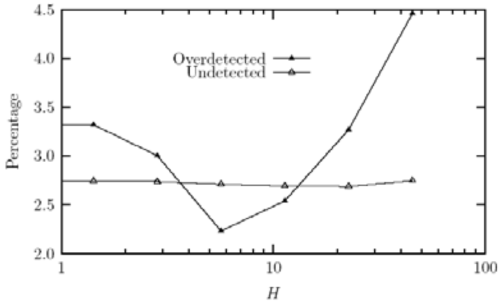

Figure 48: Effect of filter spread $H$ for Field 1 ($C = 250 \times 10-6$) with 10% Type 2 ($\Delta V/V = 25\%$, number of clusters = 1) spurious vectors for the variable threshold CNN method.[39]

Lastly, Westerweel and Scarano[40] studied probability density functions of various flows in order to identify a single universal threshold value to effectively detect spurious vectors. This was achieved by modifying the local-median filter test. Specifically, the original median residual field, defined and calculated as

$$r_i = \left| U_i - U_m \right|, \tag{48}$$

was normalized by the median $r_m$ of $\{r_1, r_2, \ldots r_8\}$

$$r_i' = \frac{\left| U_i - U_m \right|}{r_m}, \tag{49}$$

where $r_m$ is the median of the surrounding residuals. The normalized median residual was calculated for different grid turbulence data, where it was found that the corresponding histograms nearly collapsed onto a single curve (see Figure 49), suggesting that the existence of a universal probability density function. However, for regions where the turbulence levels are very low and the flow is laminar, it was found that the normalized median residual showed high values, since the normalization factor, $r_m$', approaches zero. This was compensated for by introducing a threshold, $\varepsilon$, into Equation 49, resulting in

$$r_i^* = \frac{\left| U_i - U_m \right|}{r_m + \varepsilon}. \tag{50}$$

Trial and error showed that the optimum value was ε=0.1 pixel, which interestingly corresponds to typical rms noise levels within PIV data.[41]

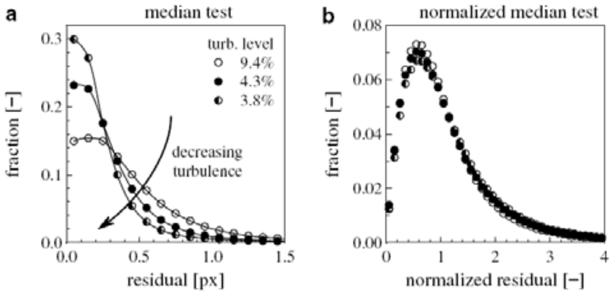

Figure 49: The histograms of the residual obtained with the conventional median test **a** and the normalized median test **b** for the grid turbulence data at decreasing turbulence levels. The histograms represent at least 99.7% of the vector data[40]

To test the universality of this approach, the histogram of the standard median residuals and normalized median residuals (Equation 50) for various flow fields ranging in Reynolds number from 0.1 to $10^7$ were calculated and plotted in Figure 50. It is clear from this figure that the probability density function does achieve a universal distribution. While the standard median test shows that the optimum residual threshold would be a function of the flow field, the normalized median test (Equation 50) shows that since the histograms almost collapse, the optimum normalized residual is independent of the flow field. Further tests show that for a single value of $r'$=2 applicable to all the tested flows, the largest 10% of the residuals and hence spurious vectors can be identified. This study, however, does not mention how many undetected and over-detected vector result from this procedure.

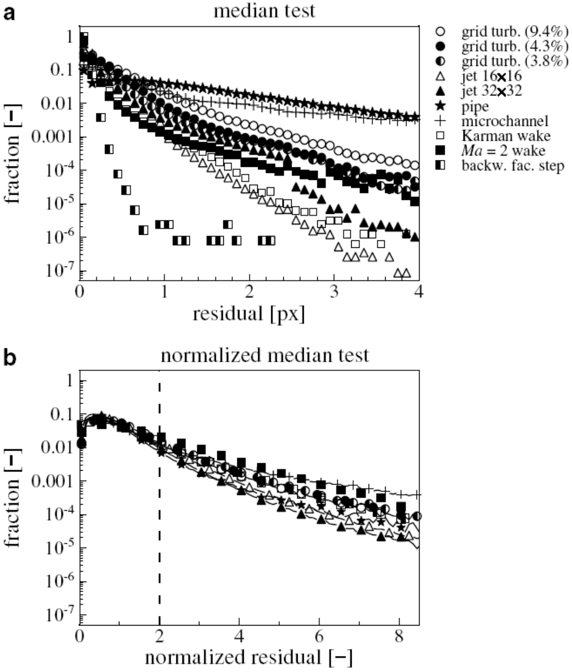

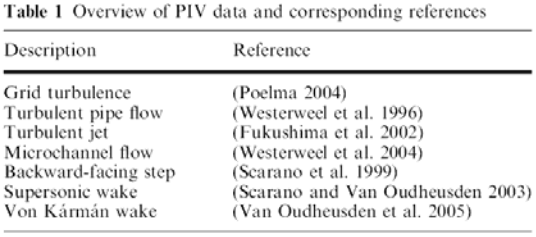

**Table 1** Overview of PIV data and corresponding references

| Description | Reference |
|---|---|
| Grid turbulence | (Poelma 2004) |
| Turbulent pipe flow | (Westerweel et al. 1996) |
| Turbulent jet | (Fukushima et al. 2002) |
| Microchannel flow | (Westerweel et al. 2004) |
| Backward-facing step | (Scarano et al. 1999) |
| Supersonic wake | (Scarano and Van Oudheusden 2003) |
| Von Kármán wake | (Van Oudheusden et al. 2005) |

Figure 50: The histograms of the residuals using the conventional median **a** and the normalized median **b** for the experimental data listed in Table 1[40]

## 2.6 Advanced PIV Methods

### *2.6.1 Window Shifting Methods*

As discussed in section 2.2, PIV provides an estimate of the true velocity, which is different from the true velocity due to noise and in-plane loss-of-pairs due to particle motion. The variation of this bias error was shown in Figure 24, and is repeated here for convenience. Upon observation, the question arises whether one can take advantage of the very small errors shown for particle shifts close to zero. In implementation, this can be done using an iterative adaptive approach. First, the image pairs are processed in a conventional manner, and then reprocessed using the initial results as a guide to adaptively shift the second window for each interrogation region. This process is iteratively repeated until convergence is achieved. Keane and Adrian[14] first proposed using a window offset equal to the particle displacement. They also recommended using a larger second interrogation window to avoid in-plane loss-of-pair. In this manner, $F_I$, the term representing the in-plane loss-of-pair (Equation 16), is maximized, causing $R_D$, the term representing the displacement correlation peak (Equation 15) to be maximized as well (see Figure 11 center and bottom). Westerweel *et al.*[21], using discrete offsetting of the same size windows, showed its effectiveness in reducing noise. Figure 51 best shows these results. With window shifting, the noise reduction in the PIV data is so great that its spectrum's noise level drops by an order of magnitude, agreeing quite nicely with the LDV data provided by Comte-Bellot and Corrsin[42].

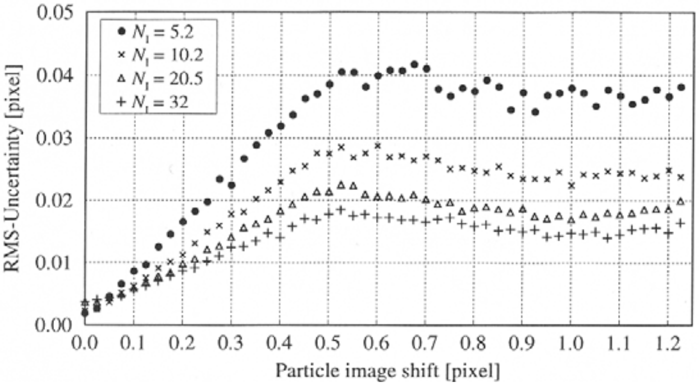

Figure 24: Measurement uncertainty for single exposure/double frame PIV as a function of particle image shift for various particle image densities $N_I$. (simulation parameters: FFT-based correlations, $d_\tau$=2.2 pixels, quantization level = 8 bits/pixel, 32 x 32 pixel interrogation window size, no noise, optimum exposure, top-hat light sheet profile.)[4]

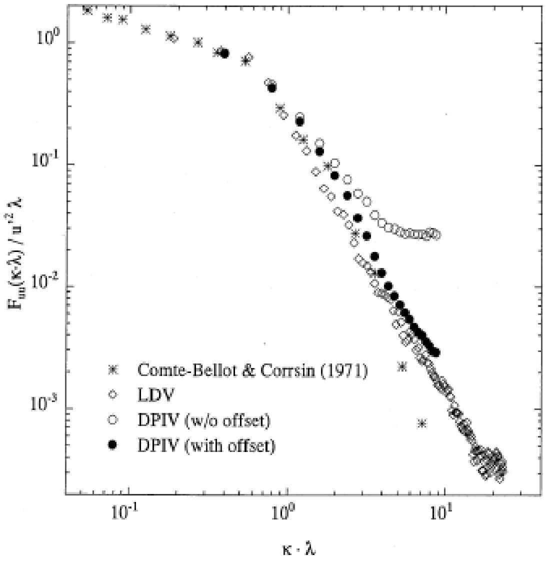

Figure 51: The normalized power spectrum of the fluctuating streamwise velocity of a turbulent flow behind a grid (at 40 grid-mesh lengths away from the grid). The open dots represent the result obtained with PIV without window offset; the closed dots the same image data but now with window offset. Also plotted are the result obtained with LDV (◊) in the same facility and at the same location as for the PIV, and the result obtained with hot-wire anemometry (x) by Comte-Bellot and Corrsin[21]

Wereley and Meinhert[43] recognized that by keeping the first window fixed and shifting the second window, one would be implementing a forward difference interrogation (FDI) algorithm,

$$\left.\frac{d\vec{X}}{d\tau}\right|_{\tau=t} = \frac{\vec{X}(t+\Delta t)-\vec{X}(t)}{\Delta t} + \frac{\Delta t}{2}\left.\frac{d^2\vec{X}}{d\tau^2}\right|_{\tau=t} + \cdots, \tag{51}$$

where the images are recorded at times *t* and *Δt*. For better accuracy, they have suggested using a central difference interrogation (CDI) algorithm,

$$\left.\frac{d\vec{X}}{d\tau}\right|_{\tau=t} = \frac{\vec{X}\left(t+\Delta t/2\right)-\vec{X}\left(t-\Delta t/2\right)}{\Delta t} + \frac{\left(\Delta t\right)^2}{24}\left.\frac{d^3\vec{X}}{d\tau^3}\right|_{\tau=t} + \cdots, \tag{52}$$

where the images are recorded at times *t-Δt/2* and *t+Δt/2*. For FDI, the velocity approximation is accurate to order *Δt*, while for the CDI, the velocity approximation is accurate to order $\Delta t^2$. In implementation, the first image's interrogation windows are shifted by an amount $-\vec{V}\left(\vec{x}\right)\Delta t/2$, while the second image's interrogation windows are shifted by an amount $\vec{V}\left(\vec{x}\right)\Delta t/2$. In practice, the amount of shift is first estimated by initially processing the images using conventional PIV, and using its results as guide for implementing the CDI routine. Wereley and Meinhert show that within 5 iterations, the solutions converge.

Gui and Wereley[44] also recognized that even with discrete window shifting using the CDI method, a zero displacement (see Figure 24) within the correlation domain could never be achieved, since almost all shifts are never perfect integer values. Consequently, they developed a continuous window shifting routine using a bilinear interpolator to allow for fractional pixel shifts. Using synthetically generated images, they tested an FFT-accelerated non-shifting correlation-based algorithm (FCTR), a discrete window shifting correlation-based interrogation algorithm (CDWS), and the continuous window shifting correlation-based interrogation algorithm (CCWS). They then documented the influences of bias and random errors, images with and without random background noise, particle image size, and particle image number density. Figure 52 shows the bias and random errors for noiseless PIV images. Clearly, the CCWS algorithm outperforms the FCTR and the CDWS algorithms by almost a factor of 5, producing a maximum bias and random error of ~.005 pixels and ~.025 pixels, respectively. Figure 53 shows the bias and random errors for noisy PIV images. This figure also shows that the CCWS algorithm outperforms the FCTR and the CDWS algorithms by almost a factor of 5 for the bias errors, and a factor of 3 for the random error. Here, the noise has an effect on the random error, since for the CCDW algorithm the random error is ~0.03, whereas for the noiseless image, it is near zero. Also seen is that for all three algorithms, the behavior of the bias error is near identical for both the noisy and noiseless images.

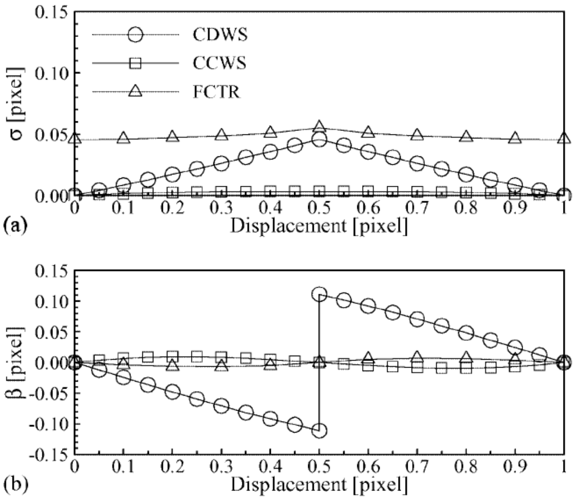

Figure 52: Random errors **a** and bias errors **b** of different algorithms for PIV images without background noise[44]

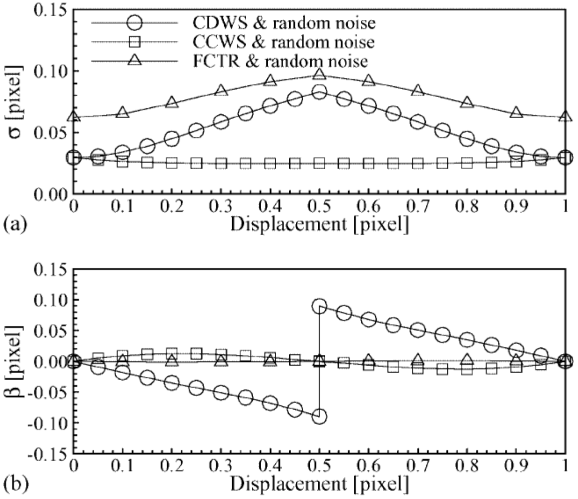

Figure 53: Random errors **a** and bias errors **b** of different algorithms[44]

Figure 54 shows the influence of the particle image size on the peak-locking (Figure 54a) and the total error (Figure 54b) for each of the algorithms. These figures show that for particle image diameters greater than 2, the peak-locking effect is minimized. For the effect on the total errors, both the FCTR and the CDWS algorithms show a minimum effect for particle image diameters ~1.5 pixels. However, for the CCWS algorithm, the total error is nearly identical to the other algorithms for particle diameters less than 1.5 pixels, but continues to decrease for increasing particle diameters.

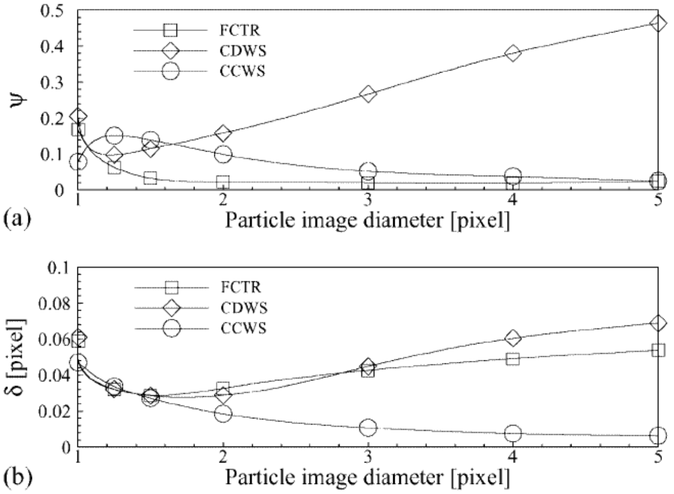

Figure 54: Influence of particle image size on: **a** peak-locking factor; **b** total error[44]

Figure 55a shows that the particle image number density has no effect on the peak-locking effect for each of the algorithms, but that its effect is the least for the CCWS algorithm. However, Figure 55b the total errors decrease with increasing particle image number density for all algorithms, being the least for the CCWS algorithm. Figure 56a shows the effect of the interrogation window size on the peak-locking effect for each of the algorithms. The size of the interrogation window has the largest effect on peak-locking for the CDWS algorithm. The least effect is seen in the FCTR algorithm, and for the CCWS algorithm, the effect of the interrogation window is slight, with a slightly increasing effect with increasing window size. The effect of the interrogation window on the total error, as shown in Figure 56b, is seen to be the least with the CCWS algorithm, being almost constant for all interrogation window sizes tested. Gui and Wereley also tested their algorithms on a thermal convection flow, where they show the histogram of the resulting PIV vectors in Figure 57. In this figure, it can be clearly seen that the FDTR and the CDWS algorithms show a very strong peak-locking effect, while the CCWS algorithm does not show any evident peak-locking effects.

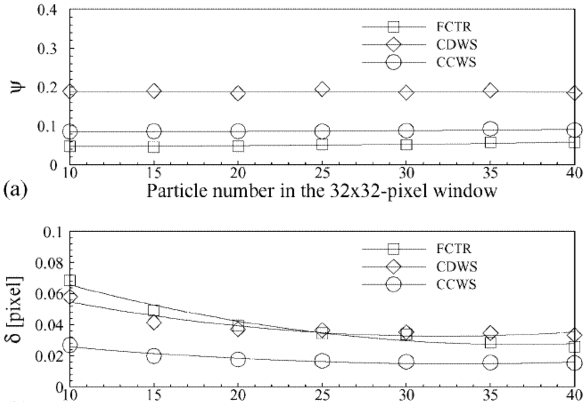

Figure 55: Influence of particle image number on: **a** peak-locking factor; **b** total error[44]

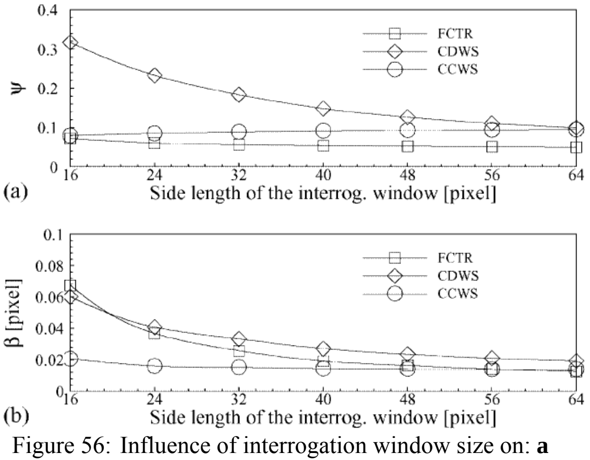

Figure 56: Influence of interrogation window size on: **a** peak-locking factor; **b** total error[44]

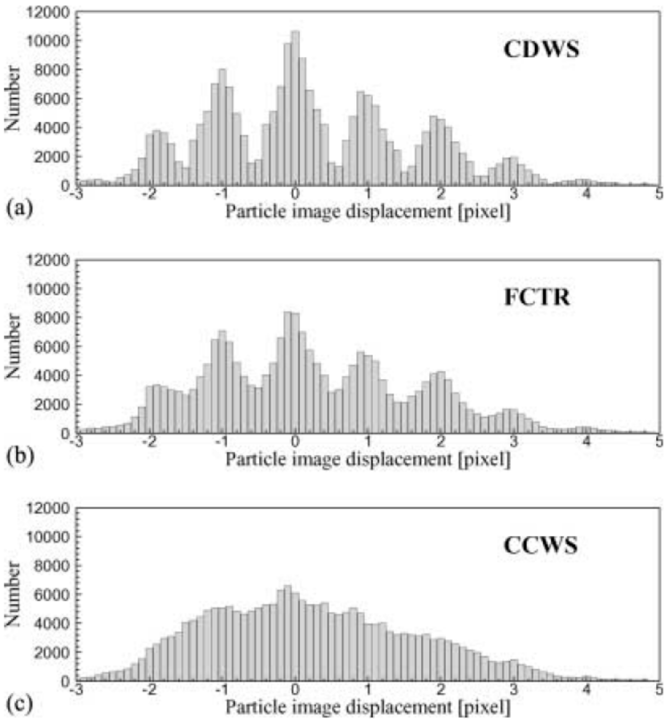

Figure 57: Histograms of particle image displacements for evaluating the PIV recording pair of the thermal convection flow with different algorithms: **a** CDWS; **b** FCTR; **c** CCWS[44]

### *2.6.2 Image Deformation Methods*

While the window shifting methods discussed in the previous section have been most helpful in reducing the uncertainty in PIV measurements, upon the inception of digital PIV[10], Huang *et al.*[45,46] recognized that motion can be decomposed into *translation* + *rotation* (a function of *du/dy and dv/dx*) + *stretch* (a function of *du/dx and dv/dy*). They consequently suggested a Particle Image Distortion (PID) technique, whereby through bilinear interpolation, the interrogation windows were distorted in the latter two terms in order to maximize on the correlation coefficient. Jambunathan *et al.*[47] also recommended a similar procedure with the exception that the second image, rather than each of the interrogation windows, was rebuilt using a bilinear interpolator. While these results showed preliminary promising results, they were not pursued vigorously, perhaps due to the computational cost necessary for image deformation. Furthermore, Huang *et al.* and Jambunathan *et al.* both reported instabilities in the convergence of their software; Huang *et al.* fixed this by smoothing their results after each iteration, while Jambunathan *et al.* fixed this by setting a condition requiring that each iterated peak calculation be larger than the previous calculation.

Through the use of a proper weighting function, Nogueira *et al.*[48,49,50,51,52,53] have been able to not only remedy the algorithm instability, but also produce a method whereby the results are more accurate and better spatially resolved. In their first work, they observed that the amplification response of a top hat window, *r*, of the wavelengths being measured showed a phase reversal such that the amplification factor became negative, and were able to show that the algorithm instabilities seen by Huang *et al.* and Jambunathan *et al.* was due to this phase reversal (see Figure 58).

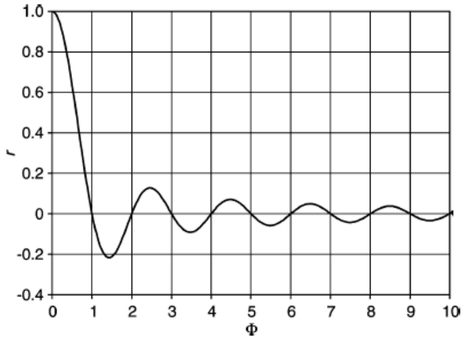

Figure 58: 1D view of the frequency response of the moving average window[48]

They also show that for the *nth* iterative corrective step, the error will be

$$\varepsilon_n = A_i\left(1-r\right)^n, \tag{53}$$

where $A_i$ is the original displacement amplitude to be measured. To ensure that the error goes to zero, the condition $0<r<2$ must hold. To correct for this phase reversal, they suggest using a symmetric weighting function

$$W\left(\xi,\eta\right) = \sum_{i,j=0}^{\infty} \mu_{ij} \cos\left(\frac{2\pi i\xi}{F}\right)\cos\left(\frac{2\pi j\eta}{F}\right) \quad \left|\xi\right|,\left|\eta\right| \le F/2, \tag{54}$$

which, under the restriction of $0<r<2$, becomes

$$W\left(\xi,\eta\right) = 9\left(4\left|\frac{\xi}{F}\right|^2 - 4\left|\frac{\xi}{F}\right| + 1\right)\left(4\left|\frac{\eta}{F}\right|^2 - 4\left|\frac{\eta}{F}\right| + 1\right), \tag{55}$$

where $F$ is the window size, and $(\xi,\eta)$ denote the coordinates from the center of the window. Graphically, the weighting function and its frequency response is shown in Figure 59.

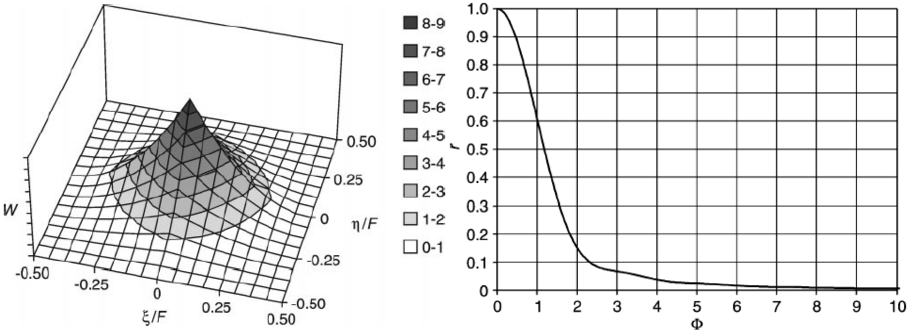

Figure 59: (left) Weighting function according to Equation 55; (right) 1D view of the frequency response of the moving average window, weighted with expression 55[48]

An unfortunate new source of error of using this function is that particle image centers are shifted towards the highest value of the weighting function (referred to as the slippage error), thus reducing the correlation peak from what it should otherwise be. To compensate for this, values of the maximum correlation coefficient are kept track of such that if they should decrease, they will not be further iterated. Using a forward differencing scheme and a biparabolic interpolator, the correlation function

$$C\left(l,m\right) = \frac{\sum_{\xi,\eta=-F/2}^{F/2} W^2\left(\xi,\eta\right) f\left(\xi,\eta\right) g\left(\xi+l,\eta+m\right)}{\sqrt{\sum_{\xi,\eta=-F/2}^{F/2} W\left(\xi,\eta\right) f^2\left(\xi,\eta\right)}\sqrt{\sum_{\xi,\eta=-F/2}^{F/2} W\left(\xi,\eta\right) g^2\left(\xi+l,\eta+m\right)}}. \tag{56}$$

is used iteratively. This method is referred to as Local Field Correction PIV (LFCPIV), and when implemented using a multigrid approach, it is referred to as a multigrid LFCPIV. Figure 60 shows various multigrid LFCPIV results for 5 iterations. Note that 2 of the 4 LFCPIV implementations produce better results than other deformation algorithms that do not apply weighting functions.

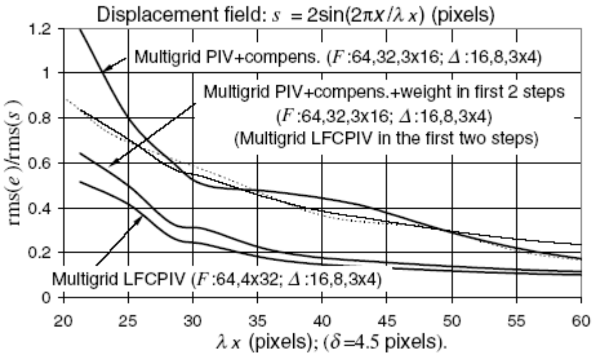

Figure 60: The performance of the five-iteration multigrid systems described in the text, together with those of the methods from Jambunathan *et al* (1995) (thin full line) and Scarano and Riethmuller (2000) (thin broken line).[50]

By using a central difference scheme instead of the forward difference scheme, keeping better track of the slippage error, and only using a single size window (64 by 64 pixels), Figure 61 shows that the uncertainties are even lower than those previously shown.

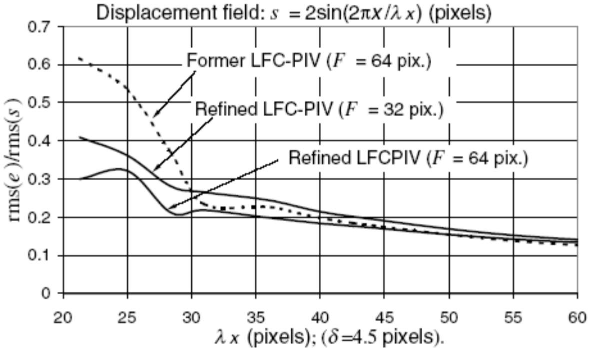

Figure 61: Performances of LFCPIV systems for the displacement fields indicated.[50]

While the weighting function in Equation 55 helps significantly reduce errors, it is by no means the only weighting function that can be used. In this regard, Nogueira *et al.*[53] studied two other weighting functions:

$$W(\xi,\eta)=\frac{24}{\pi}\left(4\left|\frac{\sqrt{\xi^2+\eta^2}}{F}\right|^2-4\left|\frac{\sqrt{\xi^2+\eta^2}}{F}\right|+1\right), \qquad (57)$$

$$if\ \left|\frac{\sqrt{\xi^2+\eta^2}}{F}\right|^2<0.5 \quad W=0$$

and

$$W(\xi,\eta)=\begin{pmatrix}12\left|\frac{\xi}{F}\right|^2-12\left|\frac{\xi}{F}\right|+3+0.15\cos\left(4\pi\xi/F\right)+0.2\cos\left(6\pi\xi/F\right)\\+0.1\cos\left(8\pi\xi/F\right)+0.05\cos\left(10\pi\xi/F\right)\end{pmatrix}$$
$$\times\begin{pmatrix}12\left|\frac{\eta}{F}\right|^2-12\left|\frac{\eta}{F}\right|+3+0.15\cos\left(4\pi\eta/F\right)+0.2\cos\left(6\pi\eta/F\right)\\+0.1\cos\left(8\pi\eta/F\right)+0.05\cos\left(10\pi\eta/F\right)\end{pmatrix} \qquad (58)$$

Equation 57 was chosen to test the asymmetric version of Equation 55, and Equation 58 was chosen to increase the frequency response for the wavelengths between F/2 and F/5. Their uncertainties as a function of iteration are shown in Figure 62, where Equation 58 is seen to have the best performance. In application to real images (see Figure 63), however, it can be seen that all three weighting functions perform satisfactorily, perhaps due to the equalizing effect of noise within the PIV images

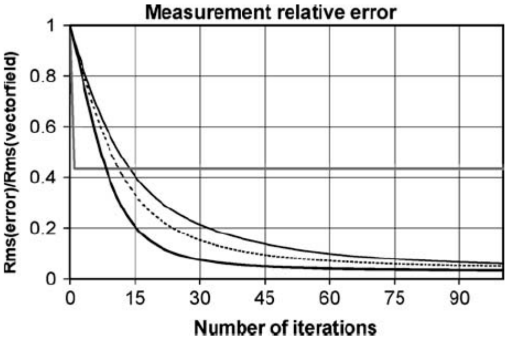

Figure 62: Comparison of algorithms. The thick horizontal line corresponds to a single-pass PIV with a 16x16-pixel non-weighted interrogation window. The smooth curves correspond to the iterative algorithms described in this section. The upper curve corresponds to Eq. 57, the middle curve to Eq. 55 and the lower curve to Eq. 58.[53]

.

Rather than use a bilinear interpolator, Scarano and Riethmuller[54], using a multigrid approach, incorporated a cardinal function interpolator

$$R(x,y)=\sum_{i,j=-F/2}^{F/2} f(i,j)\frac{\sin\left[\pi(i-x)\right]}{\pi(i-x)}\frac{\sin\left[\pi(j-y)\right]}{\pi(j-y)}, \tag{59}$$

where *R(x,y)* is the image intensity at the sub-pixel location *(x,y)*, in order to avoid or limit the loss of information in the re-sampling process[55]. The results show a significant improvement over conventional PIV and window-shifting PIV methods, however, not quite as good as the LFCPIV methods (see Figure 60).

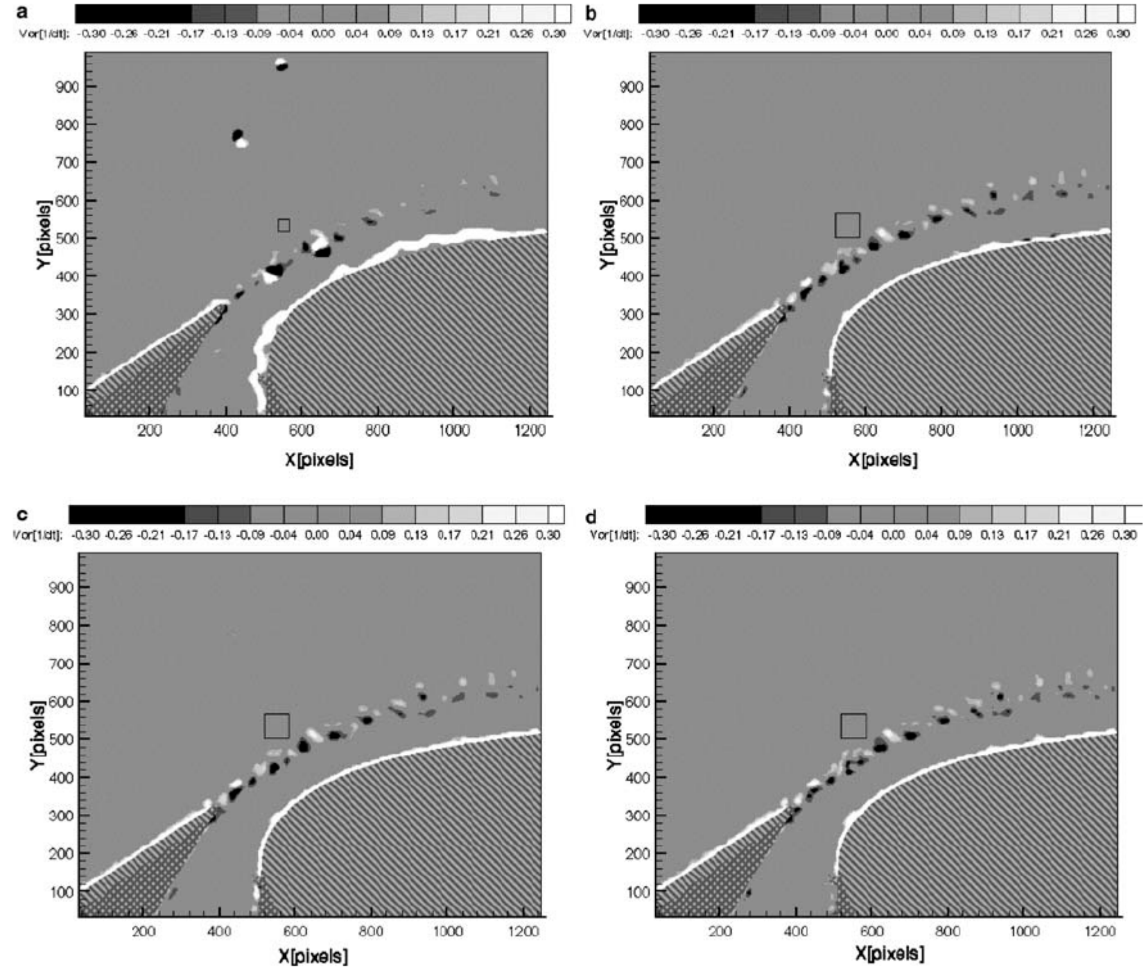

Figure 63: **a–d** Performance comparison on real images from an industrial facility. The hatched pattern indicates solid objects; the cross-hatched pattern indicates places where reflections and shadows suppress all data. **a** Vorticity plot obtained from conventional PIV data. The size of the interrogation window (32x32 pixels) is indicated by a dark box. **b** Vorticity plot obtained from LFC-PIV data with a 64x64-pixel interrogation window weighted by Eq. 55. **c** Same as **b**, but using Eq. 57. **d** Same as **b**, but using Eq. 58[53]

As indicated in this discussion so far, deforming the images is a key factor in deformation PIV methods. Towards this end, several researchers have studied the impact of various interpolation methods on the accuracy of the resulting PIV vectors, and the time necessary to calculate them. The first such study was performed by Astarita and Cardone[56], where using synthetic noiseless images with translational shifts only, they studied the bias and random uncertainties of different interpolation schemes as well as the time necessary for measurement convergence. The interpolators studied were B-spline, FFT, Cardinal interpolator based on the sinc function, bilinear, bicubic, biquadratic, simplex, and discrete window offset (IDWOS) algorithms. For the B-spline, FFT, Cardinal interpolators, the grid sizes tested for interpolation ranged from 2x2 through 16x16, 3x3 through 16x16, 4x4 through 16x16, respectively. Their results are best summarized in Figure 64, where the average bias error and total error are shown in Figure 64a and Figure 64b, respectively. These averaged values were obtained by averaging the absolute value of the errors in the displacement interval from zero to 4 pixels. In general, it can be seen that the simpler and less computationally intensive schemes (IDWOS, bilinear, bicubic, simplex) produce results that are not as accurate as schemes that are more computationally intensive (B-spline, FFT, sinc with interpolation grid sizes 6x6 through 16x16). It is interesting to note that of the latter, the B-spline algorithms give the lowest total mean uncertainties in the shortest duration of time.

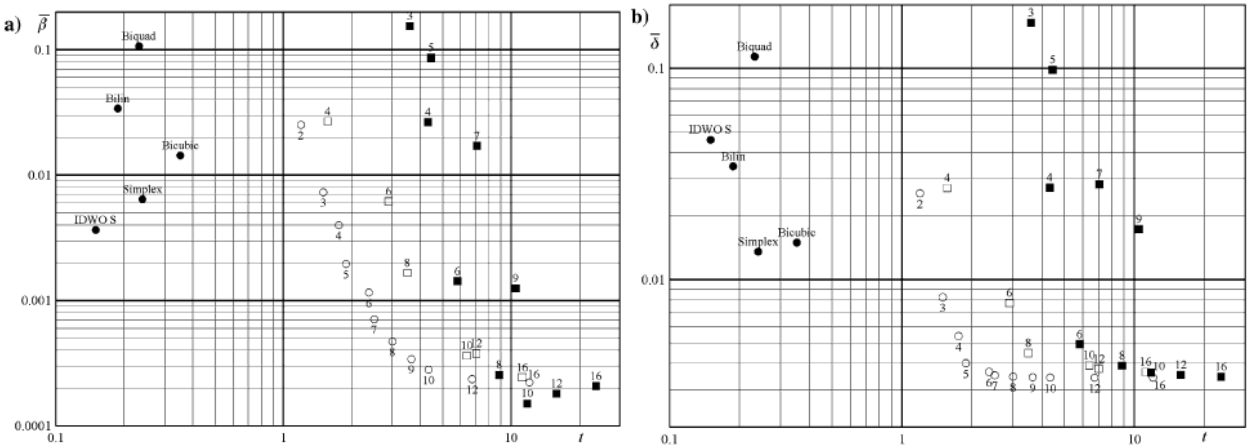

Figure 64: Bias **a** and total **b** mean errors as a function of time for various IS. Closed circles indicate high speed methods, open circles BSPL IS (the number indicates the spline order), closed squares and open squares FFT and SINC interpolation schemes (the number indicates the stencil linear dimension), respectively. The time scales are arbitrary.[56]

While useful, this study did not investigate the effects of these interpolation algorithms on non-translational motion. Towards this end, Kim and Sung[57] further assessed various interpolation schemes by considering both uniform and sheared displacements. In this study, they investigated bilinear, biquadratic, B-spline, cubic, sinc, Lagrange and Gaussian interpolations using artificially generated noiseless images with different sized particle images. The best results for the uniform displacements are shown in Figure 65 through Figure 67. The top plot in each figure shows the bias error as a function of displacement, which for all cases shows a sinusoidal behavior, while the bottom plot in each figure shows the random error as a function of displacement. It is seen that the results show the least uncertainties for the largest particle image size studied (4.4 pixels). For this particle image diameter, it is seen that the cubic (a=-0.61), Lagrange (N=6), sinc (N=10), and Gaussian (N=6) interpolation schemes have a maximum random error of .005 pixels. Of these interpolation schemes, however, the maximum bias error of the Gaussian scheme seems to be almost twice as large as the others.

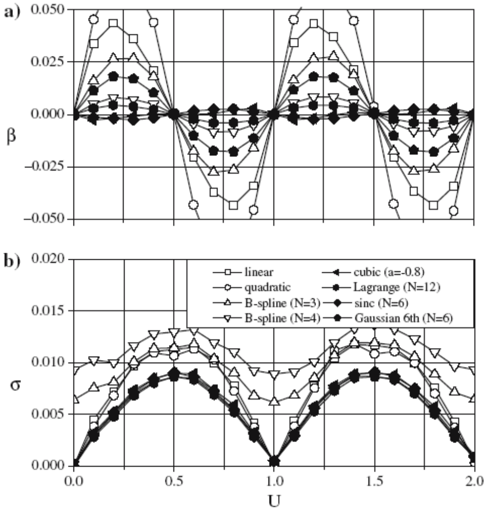

Figure 65: Comparison of the best performance for each interpolation for uniform flow ($d_p$ = 2.2 pixel)[57]

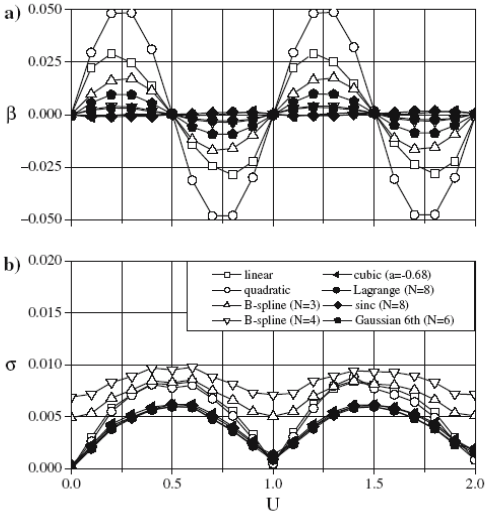

Figure 66: Comparison of the best performance for each interpolation for uniform flow ($d_p$ = 3.3 pixel)[57]

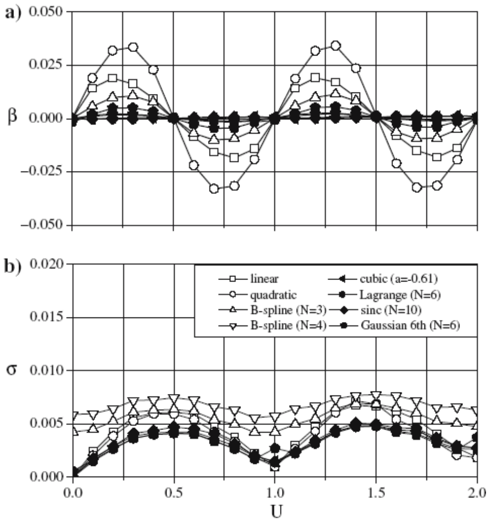

Figure 67: Comparison of the best performance for each interpolation for uniform flow ($d_p$ = 4.4 pixel)[57]

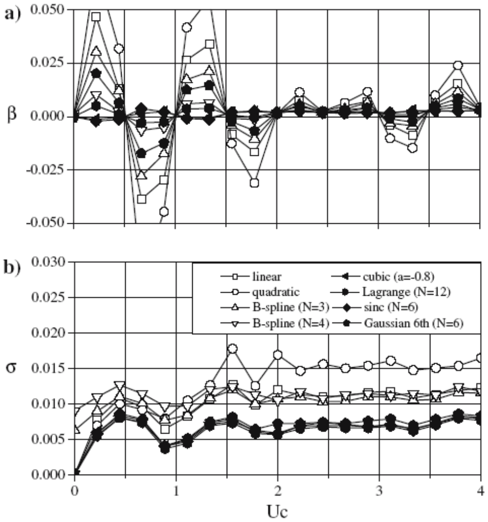

Figure 68: Comparison of the best performance for each interpolation for shear flow ($d_p$ = 2.2 pixel)[57]

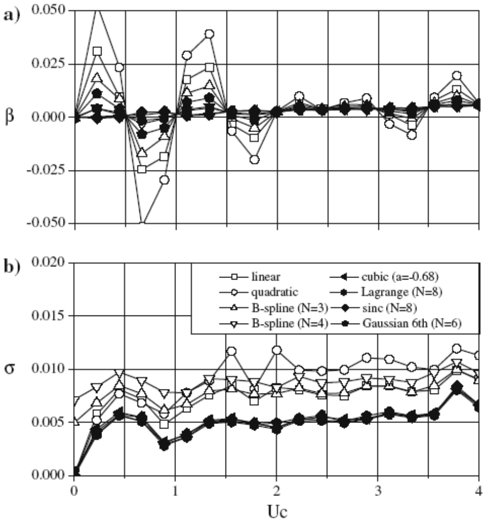

Figure 69: Comparison of the best performance for each interpolation for shear flow ($d_p$ = 3.3 pixel)[57]

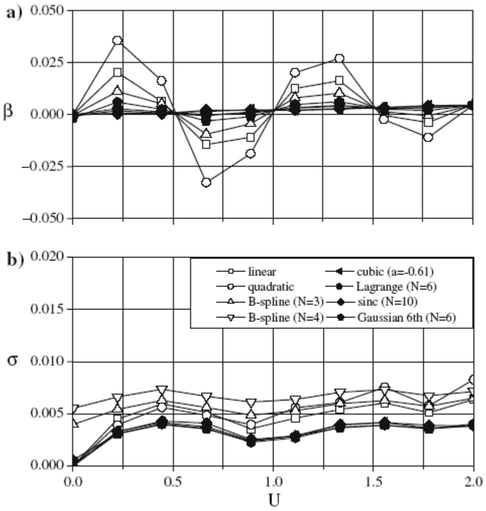

Figure 70: Comparison of the best performance for each interpolation for shear flow ($d_p$ = 4.4 pixel)[57]

The best results for the shear displacements are shown in Figure 68 through Figure 70. The top plot in each figure shows the bias error as a function of mean displacement, which for all cases shows a decaying sinusoidal behaviour, while the bottom plot in each figure shows the random error as a function of mean displacement. It is seen that the results show the least uncertainties for the largest particle image size studied (4.4 pixels). For this particle image diameter, it is seen that the cubic (a=-0.61), Lagrange (N=6), sinc (N=10), and Gaussian (N=6) interpolation schemes have a maximum random error of .004 pixels. Of these interpolation schemes, however, the maximum bias error of the Gaussian scheme seems to be almost twice as large as the others, similar to the uniform displacement results.

Also instructive is the computational time required of the interpolation schemes. Table 3 shows the ratio of the computational time to the bilinear interpolation scheme. It can be seen that for the best performing schemes, the sinc (N=10) and the Lagrange (N=6), the computation times are 27.1 and 15.5 time larger than the bilinear scheme. While the increase in computational time due to the use of deformation methods (especially the more accurate schemes) may seem large and therefore a hindrance, it should be pointed out that the rapid increase of computer processing speeds over time and the need for generating more accurate results at higher grid resolutions easily justifies using such schemes.

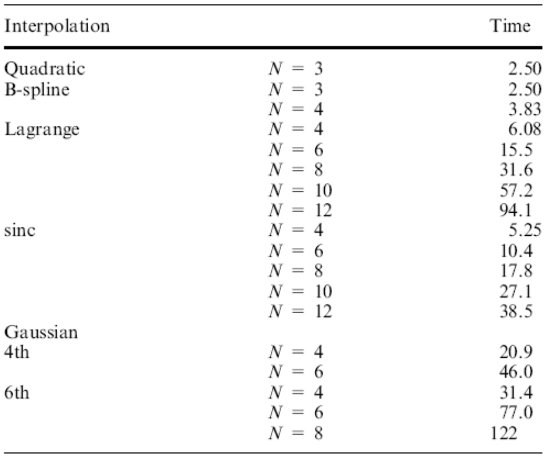

| Interpolation | | Time |
|---|---|---|
| Quadratic | $N = 3$ | 2.50 |
| B-spline | $N = 3$ | 2.50 |
| | $N = 4$ | 3.83 |
| Lagrange | $N = 4$ | 6.08 |
| | $N = 6$ | 15.5 |
| | $N = 8$ | 31.6 |
| | $N = 10$ | 57.2 |
| | $N = 12$ | 94.1 |
| sinc | $N = 4$ | 5.25 |
| | $N = 6$ | 10.4 |
| | $N = 8$ | 17.8 |
| | $N = 10$ | 27.1 |
| | $N = 12$ | 38.5 |
| Gaussian | | |
| 4th | $N = 4$ | 20.9 |
| | $N = 6$ | 46.0 |
| 6th | $N = 4$ | 31.4 |
| | $N = 6$ | 77.0 |
| | $N = 8$ | 122 |

Table 3: Ratio of computation time between each interpolation scheme to the bilinear interpolation scheme for a single iteration[57]

## 3 3-D VOLUMETRIC MEASUREMENTS

While 2D PIV provides a valuable tool for studying fluid flow, it is still limited as they are confined to measurements within a plane. To study complex three-dimensional flows therefore requires methods that will allow measurements of three-component velocity vectors within a volume. Furthermore, if such studies are transient phenomena, then these methods must allow for sequential measurements through time. While several techniques have been developed that acquire three-dimensional data by scanning the light sheet through the desired volume (Brucker[58,59]), to date, two techniques have stood out that are capable of true three-dimensional measurements. The first technique employs multiple cameras while the second employs holographic methods.

The hardware necessary for data acquisition is almost identical to those of PIV systems. The important items are bulleted below:

- The tracer particles used should be small enough to accurately follow the flow, yet large enough to provide sufficient light scattering. The particle response time as described by Equation 2 can be used to determine appropriate sizes of particles.
- The illumination source should be pulsed in order to freeze the particle motions. Both lasers and strobe lights have been successfully used. The pulses should be synchronous with the camera for proper exposure and therefore correct data acquisition. The illumination should be such that there is homogeneous illumination throughout the interrogation volume. The illumination spectra should be within the CCD's detectable spectral range. The illumination source should be bright enough to provide a good signal, especially for small tracers. This is more important for volumetric methods than for planar methods when using lasers,

since the laser beam must be spread into a volume for the volumetric methods, rather than a sheet for the planar methods.

- Digital high-resolution cameras (1K*1K or 2K*2K) are preferred in order to image higher number of particles, and also to allow for automated processing. While film provides higher resolution, its methods are extremely time-consuming for processing.
- Acquisition of digital images is done through the use of a framegrabber. Images can be stored onto RAM in real-time, but are limited to the maximum amount of RAM that can be put onto the host computer. Images can also be stored onto a real time disk. Typically disk arrays with special configurations using RAID controllers can be used to acquire massive amounts of data. If analog cameras are used, either laser disc recorders or VCRs are necessary for acquisition. For processing, however, these images must be digitized, most often not at as high a resolution or signal quality as CCDs provide, thereby degrading the quality of the digitized image.

The limitation of holographic method is that this method can only provide a snap shot of the velocity field at only a single point in time, i.e. it cannot provide a sequence of data fields through time as do the multi-camera systems. In the following section one of the multi-camera systems, the Three-Dimensional Defocusing Particle Image Velocimetry (3DDPIV) method, is presented and discussed.

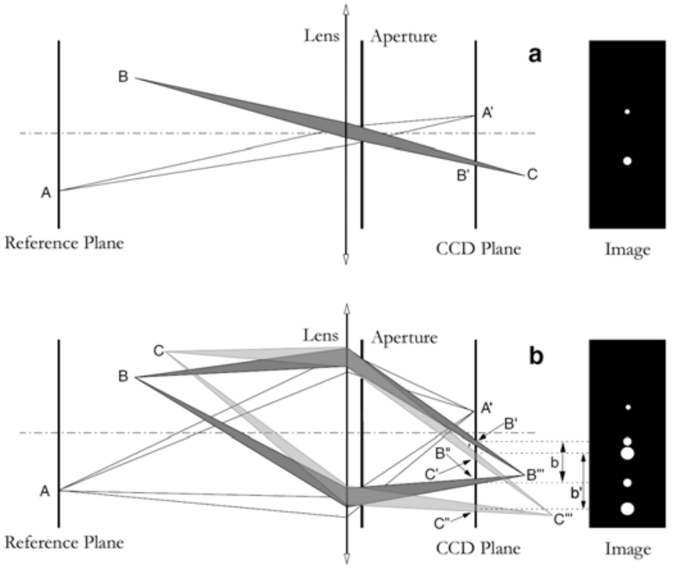

Figure 71: Diagram **a** Defocusing concept graphically demonstrated: a standard imaging set-up with aperture on-axis; **b** defocusing set-up with two off-axis apertures. Point *A* focuses from the reference plane onto *A'* on the CCD plane; point *B* focuses behind the CCD plane at point *B'''*, leaving two slightly blurred images on the CCD plane (*B'* and *B''*) at a distance *b* apart; point *C* focuses further behind the CCD plane at point *C'''*, leaving two slightly larger blurred images on the CCD plane (*C'* and *C''*) at a larger distance *b'* apart (adapted from Willert and Gharib (1992) and Pereira and Gharib (2002)).[63]

## 3.1 Three-Dimensional Defocusing Particle Image Velocimetry (3DDPIV) method

The most recent addition to the true 3D measurement methods is Defocusing Digital Particle Image Velocimetry. The concept was initially introduced by Willert & Gharib[60], and further developed and implemented by Pereira, *et al.*[61], Pereira & Gharib[62], and Kajitani & Dabiri[63]. Unlike the previous method, which is based on triangulation, this method is based on imaging with a single lens within its defocused range. This system differs from 3D particle tracking methods in that the optics in this method share one optical axis, consistent with the original concept, thus eliminating the need for complex schemes to identify particles through triangulation. Out-of-plane to in-plane error ratios using this methods are 4-6, with in-plane errors similar to those found in planar PIV techniques.

### 3.1.1 *The Defocusing Principle*

This method is best described by using a two-dimensional representation of the imaging system shown in Figure 71a, which will demonstrate the defocusing concept used to acquire 3D information. Rays from point *A* focus onto point *A'* on the image plane. Rays from *B* (off the reference plane), while still traveling through the aperture, focus away from the image plane onto *C*, leaving a blurred image, *B'*, on the image plane. Using the blurring, one can get information about a particle's position in space. In Figure 71b, the aperture is replaced with another that has two apertures equally off-axis. This time, rays from *A* travel through both apertures, and are focused onto *A'*. Likewise, rays from *B*, focus off the image plane, onto *B'''*. Because the apertures are off-axis, as the rays converge onto point *B'''*, they leave two blurred spots on the image plane, *B'* and *B''*. The separation between *B'* and *B''* (denoted by *b)* is a function of the distance *B* from the reference plane, thus providing depth information. If a particle located at *B* were to move farther from the reference plane to *C*, rays from this particle would focus off the CCD plane, onto *C'''*, leaving two blurred spots on the CCD plane, *C'* and *C''*, separated by a distance *b'* that is larger than *b*. This geometry therefore shows that the particle image separation on the CCD plane gets larger as the particle moves farther away from the reference plane, thus providing a way to gauge the depth location.

### 3.1.2 *The Descriptive Equations*

Given this optical setup, a particle's position can be shown to be

$$X = \frac{1}{2L}\left(\frac{-2Zx_{TL}}{M} + \gamma\left(L-Z\right)\right) = \frac{1}{2L}\left(\frac{-2Zx_{TR}}{M} + \gamma\left(L-Z\right)\right) = \frac{1}{L}\left(\frac{-Zx_{B}}{M} - \gamma\left(L-Z\right)\right)$$
$$= \frac{-x_0 Z}{ML}, \quad x_0 = \frac{x_B + x_{TL} + x_{TR}}{3}$$

$$Y = \frac{1}{2L}\left(-\frac{2Zy_{TL}}{M} + d\left(L-Z\right)\right) = -\frac{1}{2L}\left(-\frac{2Zy_{TR}}{M} - d\left(L-Z\right)\right) = -\frac{Zy_{B}}{l} \tag{60}$$
$$= \frac{-y_0 Z}{ML}, \quad y_0 = \frac{y_B + y_{TL} + y_{TR}}{3}$$

$$Z = \left(\frac{1}{L} + \frac{b}{MLd}\right)^{-1} = \left(\frac{1}{L} + \frac{\zeta}{M\gamma L}\right)^{-1}$$

where *M* = geometrical magnification, *d* = distance between the centers of the apertures, and *L* = distance from the aperture plane to the reference plane, $(X,Y,Z)$ = the coordinates of the point *B* in space, and $(x_{TR},y_{TR})$, $(x_{TL},y_{TL})$ and $(x_B,y_B)$ = the blurred image coordinates for the top right, top left, and bottom coordinates, respectively, $\zeta$ = the distance from the center of this equilateral triangle to any of the particle's images that identify any vertex of the equilateral triangle (i.e. $(x_{TR},y_{TR})$), and $\gamma$ = the radial distance from the optical axis to each of the apertures. The sensitivity of this system to detect changes in the depth location of particle is given by

$$\frac{\partial b}{\partial Z} = -\frac{1}{KZ^2}, \quad K = \frac{1}{MLd}. \tag{61}$$

In practice, rather than using two pinholes, three pinholes positioned in the shape of an equilateral triangle are used. For images filled with thousands of particles, this allows more precise identification of particles. Also, for good system sensitivity, the aperture distance, *d*, must be large, which can be achieved by decreasing *K,* thereby increasing $\partial b/\partial Z$. Typically, experimental setup requirements necessitate system sensitivities such that aperture separations should be larger than the diameter of the lens. This poses a problem as obtaining custom-made large lenses can be quite costly. Furthermore, triply-exposing a CCD can cause it to overcrowd rapidly, thereby only allowing limited number of particle exposures. Therefore, rather than constructing the camera with one lens, it is possible to construct the camera with 3 separate imaging systems as shown in Figure 72. This solves the problem of over-saturating a single CCD with multiple images of many particles, while using off-the-shelf lenses for the camera design.

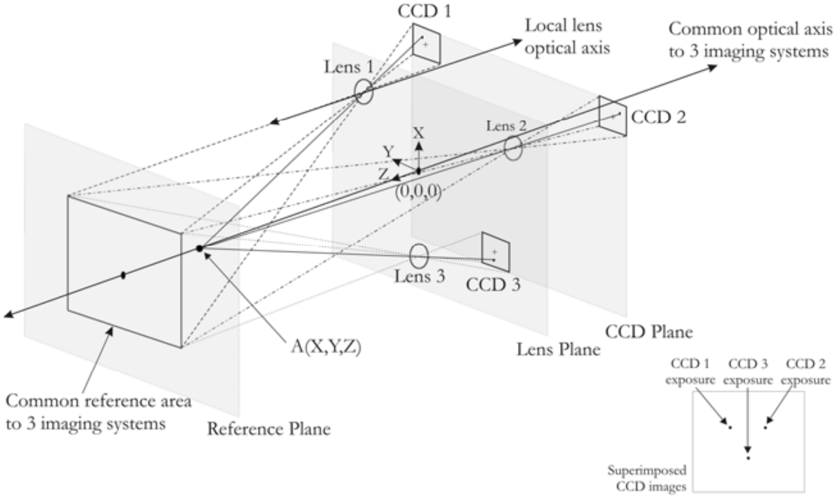

Figure 72: Implementation of 3D Defocusing PIV allowing for use of off-the-shelf hardware items[63]

### 3.1.3 *Application to flow around a propeller*

In order to test the capability of the 3DDPIV system, the flow around a propeller was imaged and mapped. Instead of using reflective particles as is done in 2D PIV systems, small bubbles (~260µm diameter) were used as flow tracers. A two-blade propeller (67 mm diameter) was rotated at 12 revolutions per second, achieving a tip velocity of 2.52 m/s within a 1 $m^3$ water tank. After phase averaging 50 velocity vectors, a three-dimensional velocity field was achieved (see Figure 73).

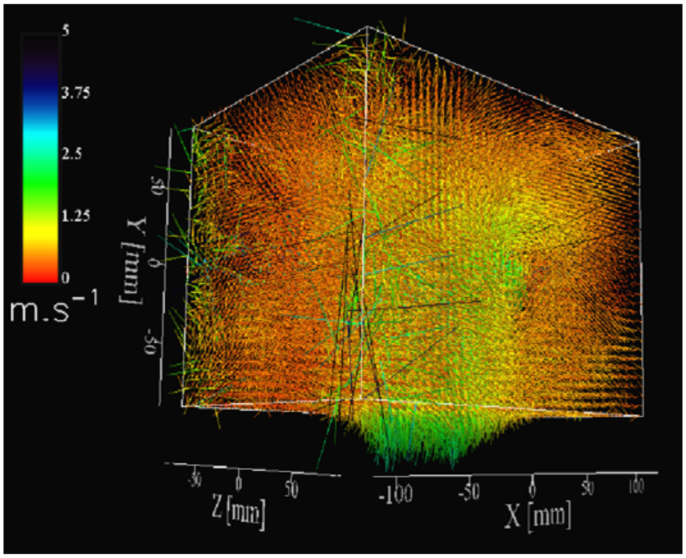

Figure 73: Three-dimensional velocity field around a rotating propeller. 3DDPIV images contain $1x10^4$-$2x10^4$ bubbles. The imaged volume is 200x200x400 $mm^3$ resulting in 72963 vectors (33*33*67 voxels).[64]

Once this velocity field was obtained and outliers were corrected for, massless particles were then numerically injected into this velocity field initially in a ring formation (Figure 74a) at one diameter upstream of the propeller, and the evolving pathlines were then observed Figure 74b,c.

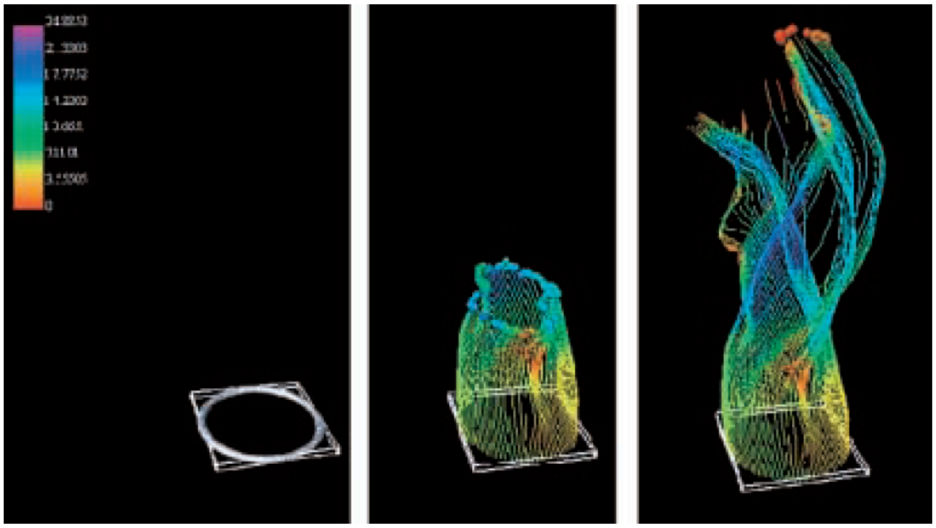

a b c

Figure 74: Pathlines of bubbles around the propeller[61]

## 4 Concluding Remarks

While the fluid dynamicist's dream of being able to measure complex, three-dimensional turbulent flow fields globally with very high spatial and temporal resolution is still far from being fully realized, the rapid developments in the various hardware and algorithmic implementations of two-dimensional cross-correlation PIV have allowed for significant insights into fluid mechanics that would have otherwise been most difficult. Two-dimensional cross-correlation PIV methods have allowed for fluid flow measurements ranging from the micrometers per seconds in micro-scale flows to supersonic speeds, in academic research to industrial applications. In addition, while single-point measurements only allowed inference to vorticity and strain rates, PIV, especially its implementation using image deformation, now allows the fluid dynamicist to directly measure these quantities globally and accurately. Most exciting is the emergence of three-dimensional methods that allow for volumetric studies of time-evolving flows, which will bring us yet a step closer to the fluid dynamicist's dream.

# 5 REFERENCES

---

[1] Tritton, D.J., 1988 Physical Fluid Dynamics, Oxford Science Publications, Oxford

[2] Brown, G.L., and Roshko, A., 1974 "On density effects and large structure in turbulent mixing layers," *J. Fluid Mech.*, 64, 775-816

[3] Guezennec, Y. G., Brodkey, R. S., Trigue, N. T., and Kent, J. C. 1994 "Algorithms for fully automated three-dimensional particle tracking velocimetry," *Exp. Fluids* 17, 209-219, ©Springer-Verlag

[4] Raffel, M., Willert, M., & Kompenhans, J. 1998, Particle Image Velocimetry, A Practical Guide, Springer-Verlag Berlin, Heidelberg, ©Springer-Verlag

[5] Merzkirch W 1974 Flow Visualization, Academic Press, New York

[6] Melling, A. 1997 "Tracer particles and seeding for particle image velocimetry", *Meas. Sci. Technol.*, 8, 12, 1406-1416

[7] Maheo, P. 1998 "Free-Surface Turbulent Shear Flows", Ph. D. Thesis, CalTech

[8] Gharib M., and Dabiri, D. 2000 "Digital Particle Image Velocimetry", Flow Visualization, Techniques and Examples, Ed. Smits A.J. and Lim T.T., Imperial College Press, Singapore

[9] Grant I., Ed. 1994 Selected Papers on Particle Image Velocimetry SPIE Milestone Series MS 99, SPIE Optical Engineering Press, Bellingham, Washington

[10] Willert, C.E., Gharib, M. 1991 "Digital Particle Image Velocimetry", *Exp. Fluids,* 10, 181-193, ©Springer-Verlag

[11] Adrian, R.J. 1991 "Particle imaging techniques for experimental fluid mechanics", *Annual Review of Fluid Mechanics*, 23, 261-304

[12] Lourenco, L. M., Krothopalli, A., and Smith, C. A. 1989, "Particle Image Velocimetry", Advances in Fluid Mechanics Measurements, Springer-Verlag, Berlin, 127

[13] Westerweel J 1993 "Digital Particle Image Velocimetry – Theory and Application", Ph.D. Thesis, Delft University Press

[14] Keane, R.D., and Adrian, R.J. 1992 "Theory of cross-correlation analysis of PIV images", *Applied Scientific Research*, 49, 191-215

[15] Adrian R J 1988 "Statistical properties of particle image velocimetry measurements in turbulent flow", *Laser Anemometry in Fluid Mechanics*, Ed R J Adrian *et al* (Lisbon: Instituto Superior Tecnico), 115–29

[16] Adrian, R.J. 1984 "Scattering particle characteristics and their effect on pulsed laser measurements of fluid flow: speckle velocimetry vs particle image velocimetry", *Appl. Opt.* 23, 1690

[17] Westerweel, J. 1997 "Fundamentals of digital particle image velocimetry", *Meas. Sci. Technol.* 8, 1379-1392

[18] Landreth, C. C., Adrian, R. J. 1988 "Electro-optical image shifting for particle image velocimetry", *Applied Optics*, 27, 4216-4220

[19] Landreth, C. C., Adrian, R. J., Yao, C. S. 1988 "Double-pulsed particle image velocimeter with directional resolution for complex flows", *Exp. Fluids*, 6, 119-128, ©Springer-Verlag

[20] Lourenco, L. M. 1993 "Velocity bias technique for particle image velocimetry measurements of high speed flows", *Applied Optics*, 32, 2159-2162

[21] Westerweel J., Dabiri D., and Gharib M. 1997 "The effect of a discrete window offset on the accuracy of cross-correlation analysis of digital PIV recordings", *Exp. Fluids*, 23, 20-28, ©Springer-Verlag

[22] Willert, C.E. 1996 "The fully digital evaluation of photographic piv recordings", *Applied Scientific Research*, 56, 79-102

---

[23] Alexander, B.F. & Ng K.C. 1991 “Elimination of systematic-error in subpixel accuracy centroid estimation”, *Opt. Eng.*, 30, 1320-1331

[24] J. Westerweel, A.A. Draad, J.G.Th. van der Hoeven & J. van Oord 1996 “Measurement of fully-developed turbulent pipe flow with digital particle image velocimetry.” *Exp. Fluids*, 20, 165-177, ©Springer-Verlag

[25] Lourenco, L. and Krothapalli A. 1995 “On the accuracy of velocity and vorticity measurements with piv”, *Exp. Fluids*, 18, 421-428, ©Springer-Verlag

[26] Prasad, A.K., Adrian, R.J., Landreth C.C., and Offutt P.W. 1992 “Effect of resolution on the speed and accuracy of particle image velocimetry interrogation”, *Exp. Fluids*, 13, 105-116, ©Springer-Verlag

[27] Roesgen T. 2003 “Optimal subpixel interpolation in particle image velocimetry”, *Exp. Fluids*, 35, 252-256, ©Springer-Verlag

[28] Nobach H. and Honkanen 2005 “Two-dimensional Gaussian regression for sub-pixel displacement estimation in particle image velocimetry or particle position estimation in particle tracking velocimetry”, *Exp. Fluids*, 38, 511-515, ©Springer-Verlag

[29] Willert, C.E. 1992: “The interaction of modulated vortex pairs with a free surface”, Ph.D. dissertation, Department of Applied Mechanics and Engineering Sciences, University of California, San Diego

[30] Fouras A. and Soria J. 1998 “Accuracy of out-of-plane vorticity measurements derived from in-plane velocity field data”, *Exp. Fluids*, 25, 409-430, ©Springer-Verlag

[31] Soria J. 1996 “An investigation of the near wake of a circular cylinder using a video-based digital cross-correlation particle image velocimetry technique”, *Exp. Thermal Fluid Sci.*, 12, 221-233

[32] Foucaut J.M. and Stanislas M. 2002 “Some considerations on the accuracy and frequency response of some derivative filters applied to particle image velocimetry vector fields”, *Meas. Sci. Technol.*, 13, 1058-1071

[33] Etebari A and Vlachos P.P 2005 “Improvements on the accuracy of derivative estimation from DPIV velocity measurements”, *Exp. Fluids*, 39, 1040-1050, ©Springer-Verlag

[34] Westerweel J 1994 “Efficient detection of spurious vectors in particle image velocimetry”, *Exp. Fluids*, 16, 236-247, ©Springer-Verlag

[35] Nogueira J., Lecuona A. and Rodriguez P.A. 1997 “Data validation, false vectors correction and derived magnitudes calculation on PIV data”, *Meas. Sci. Technol.* 8, 1493-1501.

[36] Song X., Yamamoto F., Iguchi M., and Murai Y. 1999 “A new tracking algorithm of PIV and removal of spurious vectors using Delaunay Tessellation”, *Exp. Fluids*, 26, 371-380, ©Springer-Verlag

[37] Foucaut J.M., Carlier J. and Stanislas M. 2000 “Post-processing of PIV records to allow derivative computation”, *10th Int. Symp. On Appl. Of Laser Tech. To Fluid Mech. (Lisbon)*

[38] Liang D.F., Jiang C.B., and Li Y.L. 2003 “Cellular neural network to detect spurious vectors in PIV data”, *Exp. Fluids*, 34, 52-62, ©Springer-Verlag

[39] Shinneeb A-M., Bugg J.D., and Balachandar R. 2004 “Variable threshold outlier identification in PIV data”, *Meas. Sci. Technol.*, 15, 1722-1732

[40] Westerweel J and Scarano F 2005 “Universal outlier detection for PIV data”, *Exp. Fluids*, 39, 1096-1100, ©Springer-Verlag

[41] Westerweel J 2000 “Theoretical analysis of the measurement precision on particle image velocimetry”, *Exp. Fluids*, 29, S3-S12, ©Springer-Verlag

[42] Comte-Bellot G; Corrsin S 1971 “Simple Eulerian time correlation of full and narrow-band velocity signal in grid-generated, ‘isotropic’ turbulence”, *J Fluid Mech*, 48: 273-337

[43] Meinhart, C. D., Wereley, S. T., Santiago, J. G. 1999 “PIV Measurements of a microchannel flow”, *Exp. Fluids*, 27, 414-419, ©Springer-Verlag

---

[44] Gui L., and Wereley T. 2002 “A correlation-based continuous window-shift technique to reduce the peak-locking effect in digital PIV image evaluation”, *Exp. Fluids*, 32, 506-517, ©Springer-Verlag

[45] Huang H.T., Feidler H.E. & Wang J.J. 1993 “Limitation and improvement of PIV. Part I: Limitation of conventional techniques due to deformation of particle image patterns”, *Exp. Fluids*, 15, 168-174, ©Springer-Verlag

[46] Huang H.T., Feidler H.E. & Wang J.J. 1993 “Limitation and improvement of PIV. Part II: Particle image distortion, a novel technique”, *Exp. Fluids*, 15, 168-174, ©Springer-Verlag

[47] Jambunathan K., Ju X.Y., Dobbins B.N., & Ashforth-Frost 1995 “An improved cross correlation technique for particle image velocimetry”, *Meas. Sci. Technol.*, 6, 507-514

[48] Nogueira J., Lecuona A., & Rodriguez P.A. 1999 “Local field correction PIV: on the increase of accuracy of digital PIV systems”, *Exp. Fluids*, 27, 107-116, ©Springer-Verlag

[49] Lecuona A., Nogueira J., Rodriguez P.A., Ruiz-Rivas U., & Alfaro J. 1999 “Local field correction PIV: a super-resolution technique”, *3rd Int. Workshop on PIV*, Santa Barbara, CA, USA

[50] Nogueira J., Lecuona A., & Rodriguez P.A. 2001 “Local field correction PIV, implemented by means of simple algorithms, and multigrid versions”, *Meas. Sci. Technol.*, 12, 1911-1921

[51] Nogueira J., Lecuona A., Ruiz-Rivas U., & Rodriguez P.A., 2002 “Analysis and alternatives in two-dimensional multigrid particle image velocimetry methods: application of a dedicated weighting function and symmetric direct correlation”, *Meas. Sci. Technol.*, 13, 963-974

[52] Nogueira J., Lecuona A., & Rodriguez P.A. 2005 “Limits on the resolution of correlation PIV iterative methods. Fundamentals”, *Exp. Fluids*, 39, 305-313, ©Springer-Verlag

[53] Nogueira J., Lecuona A., & Rodriguez P.A. Alfaro J.A., & Acosta A. 2005 ““Limits on the resolution of correlation PIV iterative methods. Practical implementation and design of weighting functions”, *Exp. Fluids*, 39, 314-321, ©Springer-Verlag

[54] Scarano F. & Riethmuller M.L. 2000 “Advances in iterative multigrid PIV image processing”, *Exp. Fluids*, S51-S60, ©Springer-Verlag

[55] Hall E.L. 1979 Computer image processing and recognition, Academic Press, New York

[56] Astarita T. & Cardone G. 2005 “Analysis of interpolation schemes for image deformation methods in PIV”, *Exp. Fluids*, 38, 233-243, ©Springer-Verlag

[57] Kim B.J. & Sung H.J. 2006 “A further assessment of interpolation schemes for window deformation in PIV”, *Exp. Fluids*, ©Springer-Verlag

[58] Brucker C. 1995 “digital-particle-image-velocimetry (dpiv) in a scanning light-sheet - 3d starting flow around a short cylinder”, Exp. Fluids, 19, 255-263, ©Springer-Verlag

[59] Brucker C. 1997 “3D scanning PIV applied to an air flow in a motored engine using digital high-speed video”, *Meas. Sci. Technol.*, 8, 1480-1492

[60] Willert C.E. & Gharib M (1992) “Three-dimensional particle imaging with a single camera” *Exp. Fluids*, 12, 353-358, ©Springer-Verlag

[61] Pereira F., Gharib M., Dabiri D. & Modarress D. (2000) “Defocusing digital particle image Velocimetry: a 3-dimensional DPIV measurement technique. Application to bubbly flows” *Exp. Fluids*, S78-84, ©Springer-Verlag

[62] Pereira P. & Gharib M. (2002) “Defocusing digital particle image Velocimetry and the three-dimensional characterization of two-phase flows” *Meas. Sci. Technol.*, 13, 683-694

[63] Kajitani L. & Dabiri D. 2005 “A full three-dimensional characterization of defocusing digital particle image velocimetry”, *Meas. Sci, Technol.*, 16, 790-804

[64] Courtesy of Dr. Gharib, Graduate Aeronautics Laboratory, California Institute of Technology